Aschwanden, M. J., Kontar, E. P. and Jeffrey, N. L.S. (2019) Global energetics of solar flares. VIII. The low-energy cutoff. *Astrophysical Journal*, 881(1), 1. (doi:10.3847/1538-4357/ab2cd4).

This is the author's final accepted version.

There may be differences between this version and the published version. You are advised to consult the publisher's version if you wish to cite from it.

http://eprints.gla.ac.uk/193503/

Global Energetics of Solar Flares: VIII. The Low-Energy Cutoff

Markus J. Aschwanden[1]

[1] *Lockheed Martin, Solar and Astrophysics Laboratory, Org. A021S, Bldg. 252, 3251 Hanover St., Palo Alto, CA 94304, USA; e-mail: aschwanden@lmsal.com*

Eduard P. Kontar[2] and Natasha L.S. Jeffrey[3]

[2] *School of Physics and Astronomy, University of Glasgow, G12 8QQ Glasgow, UK; e-mail: natasha.jeffrey@glasgow.ac.uk*

ABSTRACT

One of the key problems in solar flare physics is the determination of the low-energy cut-off; the value that determines the energy of nonthermal electrons and hence flare energetics. We discuss different approaches to determine the low-energy cut-off in the spectrum of accelerated electrons: (i) the total electron number model, (ii) the time-of-flight model (based on the equivalence of the time-of-flight and the collisional deflection time); (iii) the warm target model of Kontar et al. (2015), and (iv) the model of the spectral cross-over between thermal and nonthermal components. We find that the first three models are consistent with a low-energy cutoff with a mean value of ≈ 10 keV, while the cross-over model provides an upper limit for the low-energy cutoff with a mean value of ≈ 21 keV. Combining the first three models we find that the ratio of the nonthermal energy to the dissipated magnetic energy in solar flares has a mean value of $q_E = 0.57 \pm 0.08$, which is consistent with an earlier study based on the simplified approximation of the warm target model alone ($q_E = 0.51 \pm 0.17$). This study corroborates the self-consistency between three different low-energy cutoff models in the calculation of nonthermal flare energies.

Subject headings: Sun: corona — Sun: flares — magnetic reconnection

1. INTRODUCTION

The ultimate goal of this series of papers is the test of energy closure in solar flares and associated coronal mass ejection (CME) events, which entails the available energies that can be dissipated (magnetic free energy E_{mag}, and aerodynamic drag energy E_{drag}), and are transformed into primary energy dissipation processes (acceleration of nonthermal particles E_{nth}, direct heating E_{dir}, and the kinetic energy of a CME, E_{cme}), as well as into secondary processes (precipitation-induced thermal energies, and CME-accelerated particles). Statistical results of these energies have been calculated for medium-sized to large flare events (Emslie et al. 2012; Aschwanden et al. 2014, 2015; 2016; 2017; Aschwanden 2016, 2017; Aschwanden and Gopalswamy 2019). A key result is the statistical energy closure of primary energy dissipation processes, i.e., $(E_{nth} + E_{dir} + E_{cme})/E_{diss} = 0.87 \pm 0.18$) (Aschwanden et al. 2017). The largest amount of the dissipated magnetic energy goes into the acceleration of electrons $E_{nth}/E_{diss} = 0.51 \pm 0.17$. Importantly, the measurement of the nonthermal energy E_{nth} bears the largest uncertainty due to the poorly known low-energy cutoff ε_c, which is the central focus of this study.

The low-energy cutoff problem arises because the instantaneous electron injection spectrum can be approximated with a power-law function $f_e(\varepsilon) \propto \varepsilon^{-\delta}$ above a minimum electron energy ε_c (e.g., in the

thick-target model of Brown 1971). The fact that the power-law slope is generally very steep, i.e., $\delta \approx 3 - 8$ (Dennis 1985), makes the spectrally integrated electron flux extremely sensitive to the accurate value of the low-energy cutoff value ε_c. If we change this cutoff value from $\varepsilon = 10$ keV by a factor of 2 to $\varepsilon = 20$ keV, the electron flux varies by a factor of $\approx 2^\delta$, which amounts to 1-2 orders of magnitude. The effects of low-energy cutoffs on solar flare microwave and hard X-ray spectra was investigated in Holman (2003), with the finding that microwave spectra become smoothed in the optically thick portion, while hard X-ray (photon) spectra are flattened below the cutoff energy. The modeling of the thermal spectrum of hard X-ray photons has traditionally been done with an isothermal model (Culhane et al. 1969; Culhane and Acton 1970; Brown et al. 1974; Holman et al, 2011), while a multi-thermal function involves a more realistic approach and was found to fit the data equally well (e.g., Aschwanden 2007). Moreover, the altitude of the coronal X-ray sources are observed to increase with energy in the thermal range (Jeffrey et al. 2015), so that solar flares are multi-thermal and have strong vertical temperature and density gradients with a broad temperature distribution. The ambiguity between an iso-thermal and a multi-thermal spectrum contributes to further confusion between the thermal and nonthermal spectral components, so that the spectral cross-over does not reveal the exact cutoff energy, but yields a value that is about a factor of two too high. In a previous study on the multi-thermal modeling of 44 flare events, the spectral cross-over was found in the range of $e_{co} = 10 - 28$ keV, with a mean and standard deviation of $e_{co} = 18.0 \pm 3.4$ keV (Aschwanden 2007).

A new theoretical model based on collisional relaxation and diffusion of electrons in a warm coronal plasma was proposed by Kontar et al. (2015; 2019), which in principle yields the low-energy cutoff ε_{wt} in a modified thick-target model. This modified thick-target model represents a more realistic approach, because it generalizes the standard cold thick-target model (with a cold plasma target) by including an additional warm plasma "lid" above the cold chromospheric component and, unlike the cold thick-target, preserves the number of electrons in the warm plasma. Importantly, the warm target model uses the warm coronal plasma environment (its temperature, number density, and warm plasma extent) to constrain the properties of the accelerated electron distribution. In general, the low-energy cutoff should be determined by fitting the warm target model to the observed X-ray count spectrum (see Kontar et al. 2019). An application of a simplified version of this warm target model to 191 M and X-class flares yielded a mean low-energy cutoff of $\varepsilon_{wt} = 6.2 \pm 1.6$ keV (Aschwanden et al. 2016), which is significantly lower than the cross-over energy of $\varepsilon_{co} = 21 \pm 6$ keV. It can be shown that the low-energy cutoff in a cold thick-target model is essentially undetermined (e.g. Ireland et al. 2013; Kontar et al. 2019), while it was shown that the warm target model can constrain the low-energy cutoff down to 7% at a 3-σ level (Kontar et al. 2019).

Here, we study the low-energy cutoffs inferred from the warm target model further. One issue is that the plasma in a flare is highly inhomogeneous, ranging from the cold background corona values at the beginning of a flare ($T_{cold} \approx 0.5 - 2$ MK) to the hot chromospheric evaporation component ($T_{hot} \approx 5 - 25$ MK) at the flare peak time, causing some ambiguity about which temperature to attribute to the warm-plasma component that constrains the low-energy cutoff. In the warm target model, the deduction of the coronal plasma environment is crucial for constraining the low energy cutoff, and hence the nonthermal electron power (Kontar et al. (2019).

Further, we will explore the total number of electrons in a flaring plasma and the spectral cross-over ε_{co} as well as the warm target model ε_{wt} predictions. Moreover, the electron number model ε_{en}, and the electron time-of-flight model ε_{tof} will be applied. The latter two models invoke the equivalence of the collisional deflection time and the electron time-of-flight time scale, as well as the limit of the maximum number of electrons that can be accelerated in a finite flare volume, which at the same time solves the electron number problem.

The content of this paper includes an analytical description and derivation of all four theoretical models of the low-energy cutoff (Section 2), followed by a description of the data analysis and fitting of the theoretical models to the observational data sets of all M and X-class flares observed with the *Atmospheric Imaging Assembly (AIA)* and the *Helioseismic and Magnetic Imager (HMI)* onboard the *Solar Dynamics Observatory (SDO)* during 2010-2014, which amounts to 191 solar flare events (Section 3), with discussion (Section 4) and conclusions (Section 5).

2. THEORY

We describe four different models that independently provide theoretical estimates of the low-energy cutoff of a hard X-ray spectrum in solar flares. In the following, we present analytical derivations and assumptions of these models: the *electron number model* (Section 2.1), the *time-of-flight model* (Section 2.2), the *warm target model* (Section 2.3), and the *spectral cross-over model* (Section 2.4). The first two models are used here for the first time to derive the low-energy cutoff, while the third model was used in Aschwanden et al. (2016), and the fourth model represents a common method to derive upper limits on the low-energy cutoff.

2.1. The Total Electron Number Model

In the thick-target model (Brown 1971; e.g., see Section 13.2.2 in textbook Aschwanden 2004), the hard X-ray photon spectrum is defined by a power law function of the observed photon energies ϵ_x,,

$$I(\epsilon_x) = I_1 \frac{(\gamma - 1)}{\epsilon_1} \left(\frac{\epsilon_x}{\epsilon_1} \right)^{-\gamma} \qquad [\text{photons cm}^{-2} \text{ s}^{-1} \text{ keV}^{-1}] \ . \tag{1}$$

The corresponding electron injection spectrum of electrons is,

$$f_e(\varepsilon) = 2.68 \times 10^{33} \ (\gamma - 1) \ b(\gamma) \ \frac{I_1}{\epsilon_1^2} \left(\frac{\varepsilon}{\epsilon_1} \right)^{-(\gamma+1)} \qquad [\text{electrons keV}^{-1}\text{s}^{-1}] \ , \tag{2}$$

and has the power law slope $\delta = \gamma + 1$. The total number of electrons above a cutoff energy ε_c, i.e., $F(\varepsilon \geq \varepsilon_c)$, is given by the thick-target model

$$F(\varepsilon \geq \varepsilon_c) = \int_{\varepsilon_c}^{\infty} f_e(\varepsilon) \ d\varepsilon = 2.68 \times 10^{33} \ b(\gamma) \ \frac{(\gamma - 1)}{\gamma} \frac{I_1}{\epsilon_1} \left(\frac{\varepsilon}{\epsilon_1} \right)^{-\gamma} \qquad [\text{electrons s}^{-1}] \ , \tag{3}$$

where $b(\gamma)$ is an auxiliary function that contains the beta function $B(p, q)$,

$$b(\gamma) = \gamma^2 (\gamma - 1)^2 B \left(\gamma - \frac{1}{2}, \frac{3}{2} \right) \ , \tag{4}$$

which was been calculated by Hudson et al. (1978) for a relevant range of spectral slopes γ of the observed photon spectrum, and was approximated by the function (Aschwanden 2004),

$$b(\gamma) \approx 0.27 \ \gamma^3 \ , \tag{5}$$

and ϵ_1 is the reference energy at which the photon flux I_1 is measured.

Now we define the total number of electrons integrated over the total flare duration τ_{flare},

$$N_e = F(\varepsilon \geq \varepsilon_c) \, \tau_{flare} \qquad [\text{electrons}] . \qquad (6)$$

On the other side, we can assume the total number of accelerated nonthermal electrons during a flare by integrating the preflare electron density n_{e0} over the flare volume $V = L^3 q_{geo}$, where L is an appropriate length scale of a cube that encompasses the entire flare volume,

$$N_e = n_{e0}V = n_{e0} \, L^3 \, q_{geo} \qquad [\text{electrons}] , \qquad (7)$$

and q_{geo} is a geometric filling factor of the subvolume that contains the number of electrons that can be accelerated out of the cubic flare volume. We note that this assumption neglects the role of return currents, which will maintain the total number of electrons (e.g., Somov 2000). In other words, the total number of electrons in the flaring region is assumed to be equal to the total number of electrons accelerated above the low energy cut-off. Even if this approximation is coarse, it gives useful details about the efficiency of electron acceleration in solar magnetic reconnection regions.

In the standard CHSKP flare models for magnetic reconnection (Carmichael 1964; Hirayama 1974; Sturrock 1966; Kopp and Pneuman 1976), the subvolume in which charged particles (electron and ions) are accelerated encompasses about a fraction of $q_{geo} \approx 1/4$ of the cubic flare volume, as it can be estimated from the geometry shown in Fig. 1 (shaded triangular subvolume). The geometric filling factor consists of a factor of $q_{height} = 1/2$ due to the vertical cusp range that covers half of the apex height, and an additional factor of $q_{triangle} = 1/2$ that accommodates the ratio of the triangular arcade cross-section to the encompassing cube volume, resulting into a combined factor of $q_{geo} = q_{height} \times q_{triangle} = (1/2) \times (1/2) = 1/4$. Alternatively, we can estimate the geometric filling factor from the approximate size of the diffusion region of the magnetic reconnection volume, which occupies the half apex height ($h = L/2$) and half of the horizontal footpoint separation ($w_L/2$), and this way produces the same geometric filling factor of $q_{geo} = (h/L) \times (w/L) = (1/2) \times (1/2) = 1/4$ (hatched area in Fig. 1).

Combining the two expressions for the total number of electrons N_e accelerated in a flare (using Eqs. 1-6) we obtain,

$$N_e = n_e L^3 q_{geo} = 0.72 \times 10^{33} \; \gamma^2(\gamma - 1) \frac{I_1}{\epsilon_1} \left(\frac{\varepsilon_{en}}{\epsilon_1} \right)^{-\gamma} \tau_{flare} \qquad [\text{electrons}] . \qquad (8)$$

Using the normalized unit $L_{10} = L/10^{10}$ cm, we obtain the following simple expression for the low-energy cutoff ε_{en}, where the subscript "en" refers to the *electron number* model,

$$\varepsilon_{en} = \epsilon_1 \left[\frac{n_{e0} \, L_{10}^3 \, q_{geo} \, \epsilon_1}{0.72 \, \gamma^2(\gamma - 1) \, I_1 \, \tau_{flare}} \right]^{-1/\gamma} \qquad [\text{keV}] , \qquad (9)$$

which depends on the observables $n_{e0}, \gamma, I_1, \epsilon_1, \tau_{flare}$ and the model parameter $q_{geo} \approx 1/4$. The photon flux I_1 and the spectral power law slope γ at the energy ϵ_1 can directly be obtained from a hard X-ray spectrum, the flare duration τ_{flare} can be measured from hard X-ray time profiles, and the electron density n_{e0} has to be estimated before the onset of the flare, which is typically $n_{e0} \approx 10^9$ cm^{-3} (Fig. 3h).

Once we have a model for the low-energy cutoff ε_{en}, we can calculate the power in nonthermal electrons above this cutoff energy by integrating the electron energies ε, with $b(\gamma)$ defined in Eqs. (4) or (5),

$$P_{en}(\varepsilon \geq \varepsilon_{en}) = \int_{\varepsilon_{en}}^{\infty} f_e(\varepsilon) \, \varepsilon \, d\varepsilon = 4.3 \times 10^{24} \, b(\gamma) I_1 \left(\frac{\varepsilon_{en}}{\epsilon_1} \right)^{-(\gamma-1)} \qquad [\text{erg s}^{-1}] \qquad (10)$$

and the total energy E_{en} integrated over the flare duration $\tau_{flare} = (t_2 - t_1)$ is

$$E_{en} = \int_{t_1}^{t_2} P_{en}(\varepsilon \geq \varepsilon_{en}, t) \, dt \qquad [\text{erg}] \,, \tag{11}$$

where the photon flux $I_1(t)$, the power law slope $\gamma(t)$, and the low-energy cutoff energy $\varepsilon_{en}(t)$ are time-dependent.

2.2. The Time-of-Flight Model

For stochastic acceleration models with binary Coulomb collisions, where particle gain and lose energy randomly, the collisional mean free path yields an upper limit for the propagation distance of free-streaming electrons. The balance between acceleration and collisions can lead to the formation of a kappa-distribution according to some solar flare models (e.g., Bian et al. 2014). For solar flares, we can thus estimate the critical energy between collisional and collisionless electrons from the collisional deflection time t_{defl} (Benz 1993),

$$t_{defl} \approx 0.95 \times 10^8 \left(\frac{e_{keV}^{3/2}}{n_e}\right) \left(\frac{20}{\ln \Lambda}\right) \,, \tag{12}$$

where $\ln \Lambda \approx 20$ is the Coulomb logarithm. We set the collisional deflection time equal to the (relativistic) time-of-flight propagation time between the coronal acceleration site and the chromospheric thick-target energy loss site,

$$t_{tof} = \frac{L_{tof}}{v} = \frac{L_{tof}}{\beta c} \,. \tag{13}$$

The relativistic speed $\beta = v/c$,

$$\beta = \sqrt{1 - \frac{1}{\gamma_r^2}} \,, \tag{14}$$

is related to the kinetic energy e_{kin} of the electron by,

$$e_{kin} = m_e c^2 (\gamma_r - 1) = 511(\gamma_r - 1) \qquad [\text{keV}] \,, \tag{15}$$

where γ_r represents here the relativistic Lorentz factor (not to be confused with the spectral slope γ used above, i.e., Eq. (1)). We are setting these two time scales equal (Aschwanden et al. 2016, Appendix A therein),

$$t_{defl} = t_{tof} \,, \tag{16}$$

we use $\ln \Lambda \approx 20$, we define the kinetic energy $\epsilon_{keV} = \epsilon_{kin}$, and obtain with Eqs. (12-16),

$$(\gamma_r - 1)^{3/2} \left(1 - \frac{1}{\gamma_r^2}\right)^{1/2} = \frac{L_{tof} \, n_e}{0.95 \times 10^8 \times 511^{3/2} c} \,. \tag{17}$$

Using the low-relativistic approximation (for $\gamma_r \gtrsim 1$),

$$(\gamma_r - 1)^{3/2} \left(1 - \frac{1}{\gamma_r^2}\right)^{1/2} = (\gamma_r - 1)^{3/2} \frac{(\gamma_r - 1)^{1/2}(\gamma_r + 1)^{1/2}}{\gamma_r} = \frac{(\gamma_r - 1)^2(\gamma_r + 1)^{1/2}}{\gamma_r} \approx (\gamma_r - 1)^2 \sqrt{2} \,, \tag{18}$$

we obtain,

$$(\gamma_r - 1)^2 \sqrt{2} \approx 0.0003 \times \left(\frac{L_{tof}}{10^{10} \text{ cm}}\right) \left(\frac{n_e}{10^{10} \text{ cm}^{-3}}\right) \,. \tag{19}$$

The time-of-flight distance is approximately $L_{tof} = L\sqrt{2}$, where the flare length scale L is also the vertical extent of the cusp (Fig. 1), and the factor $\sqrt{2}$ corrects for the mean pitch angle ($45°$) of the electrons spiraling along the time-of-flight path. Then, by inserting $(\gamma_r - 1) = e_c/511$ keV from Eq. (15), we find the cross-over energy $e_{tof} \approx e_{kin}$, explicitly expressed,

$$e_{tof} \approx 28 \left(\frac{L}{10^{10} \text{ cm}} \right)^{1/2} \left(\frac{n_e}{10^{10} \text{ cm}^{-3}} \right)^{1/2} \qquad [\text{keV}] . \tag{20}$$

This expression requires the measurement of a mean length scale $L = A^{1/2}$ of the flare area and an average electron density n_e where flare-accelerated electrons propagate.

From the model of the low-energy cutoff energy ε_{tof}, we can calculate the power in nonthermal electrons above this cutoff energy by integrating over the electron energies ε,

$$P_{tof}(\varepsilon \geq \varepsilon_{tof}) = \int_{\varepsilon_{tof}}^{\infty} f(\varepsilon) \, d\varepsilon = 4.3 \times 10^{24} \, b(\gamma) I_1 \left(\frac{\varepsilon_{tof}}{\epsilon_1} \right)^{-(\gamma-1)} \qquad [\text{erg s}^{-1}] . \tag{21}$$

The total energy integrated over the flare duration is then, using the time-dependent functions $\gamma(t)$, $I_1(t)$, and $\varepsilon_{tof}(t)$,

$$E_{tof} = \int_{t_1}^{t_2} P_{tof}(\varepsilon \geq \varepsilon_{tof}, t) \, dt \qquad [\text{erg}] . \tag{22}$$

Turning the argument around predicts a time-of-flight distance $L_{tof} \approx \varepsilon_{tof}^2/n_e$ as a function of the low-energy cutoff ε_{tof}, which is a similar concept that has been applied to model the size L of the acceleration region as a function of the electron energy e, i.e., $(L - L_0) \propto e^2/n_e$ (Guo et al. 2012a, 2012b, 2013; Xu et al. 2008).

2.3. The Warm-Target Model

Previous applications of the thick-target model generally assume cold (chromospheric) temperatures in the electron precipitation site (e.g., Holman et al. 2011, for a review). At the same time, the temperature of the flaring solar corona is sufficiently high so that finite temperature effects must be included (Galloway et al. 2005; Goncharov et al. 2010; Jeffrey et al. 2014). Moreover, the slow spatial diffusion of thermalized electrons, previously ignored, led to the theoretical development of the warm target model (Kontar et al. 2015). The model has been tested with numerical simulations that include the effects of collisional energy diffusion, spatial transport and thermalization of fast electrons (Jeffrey et al. 2014).

The warm target model assumes a two-temperature target plasma (Kontar et al. 2015, 2019): the warm solar corona and the cold chromosphere. The warm corona is collisionally thick to electrons with energy $E < \sqrt{2KnL}$, where $K = 2\pi e^4 \ln \Lambda$ is a constant, n is the density of the coronal plasma, and L is the length of the warm target region. Therefore, the accelerated electrons injected into a flaring loop propagate and collide in the warm plasma. Electrons with energy $E^2 < 2KnL$ lose all of their energy in the coronal plasma and join the Maxwellian distribution of the surrounding plasma, increasing the density of thermal plasma in the loop. The mean electron flux spectrum can be represented by (Kontar et al. 2015),

$$\langle nVF \rangle(E) = \frac{1}{2K} E e^{-E/k_B T} \int_{E_{min}}^{E} \frac{e^{E'/kT} dE'}{E' G \left(\sqrt{\frac{E'}{k_B T}} \right)} \int_{E'}^{\infty} \dot{N}(E_0) dE_0 , \tag{23}$$

where $G(x) = [\mathrm{erf(x)} - x \; \mathrm{erf'(x)}]/2\mathrm{x}^2$. The lower limit in Eq. (23) is given by,

$$E_{min} \approx 3k_BT \left(\frac{5\lambda}{L}\right)^4 , \tag{24}$$

where $\lambda = (k_BT)^2/2Kn$ is the collisional mean free path, and Eq. (24) is determined by considering the warm plasma properties in the corona. The mean electron flux $\langle nVF \rangle(E)$ convolved with the bremsstrahlung cross-section $\sigma(E, \epsilon)$ predicts the X-ray flux spectrum at $R = 1$ AU,

$$I(\epsilon) = \frac{1}{4\pi R^2} \int_E^\infty \langle nVF \rangle(E)\sigma(E, \epsilon)dE . \tag{25}$$

where ϵ is the photon energy. Fitting the warm target model X-ray spectrum to the observed X-ray spectrum, allows us to determine the parameters of the injected electron flux spectrum, which here is assumed to be a power-law[1]

$$\dot{N}(E) = \dot{N}_0 \frac{\delta - 1}{E_c} \left(\frac{E}{E_c}\right)^{-\delta} , \tag{26}$$

where $\dot{N}_0$ is the electron acceleration rate [electrons/s], δ is the spectral index, and E_c is the low-energy cut-off in the injected electron spectrum.

The warm target model suggests that electrons are thermalized in the warm plasma of the coronal loop and produce detectable thermal emission with an emission measure of,

$$\Delta EM \approx \frac{\pi}{K}\sqrt{\frac{m_e}{8}}(k_BT)^2 \frac{\dot{N}_0}{E_{min}^{1/2}} , \tag{27}$$

where ΔEM characterizes the additional contribution to the soft X-ray emission measure from the thermalized accelerated electrons. These hot Maxwellian electrons can diffusively escape from the warm plasma of the loop and collisionally stop in the dense cold chromosphere. High-energy electrons with $E^2 > 2KnL$ behave in the same way as in the standard cold thick-target model. It is important to note that the warm target model is responsible for the nonthermal component, and for a fraction of the thermal component of the X-ray emission. The pile-up of low energy electrons thermalized in the flaring corona allows us to solve the low energy cut-off problem (Kontar et al. 2019) by comparing the thermalized electrons, that is, by determining the contribution from Eq. (27) and the observed X-ray spectrum. In other words, if the low-energy cutoff is determined too low (i.e. if the contribution from Δ EM is too large), then the warm target model produces too many thermalized electrons and hence can be ruled out.

According to the warm-target model of Kontar et al. (2015), the effective low-energy cutoff $E_c \simeq \varepsilon_{wt}$ can be coarsely approximated as

$$\varepsilon_{wt} \approx (\xi + 2)k_BT_e = \delta \; k_BT_e , \tag{28}$$

where $\xi = \gamma - 1$ is the power-law slope of the source-integrated mean electron flux spectrum (see Eqs. (8)-(10) in Kontar et al. 2015), and T_e is the temperature of the warm target plasma. For medium-sized to large X-class flares, this temperature range spans $T_e \approx 10 - 30$ MK, giving (in energy units) $e_{th} = k_BT_e = 0.9 - 2.6$ keV, and for a typical value of the photon spectral slope $\delta = \gamma + 1 \approx 4$, low-energy cutoffs of $e_{th} = \delta \; k_BT_e \approx 3.5 - 8.5$ keV are predicted. In this simplified version, Kontar et al. (2015) stress that the value of T_e used must be the value of T_e corresponding to the Maxwellian thermal plasma in the loop.

---

[1]A warm target kappa model is also available in OSPEX (see Kontar et al. (2019)).

Further, we stress that Eq. (28) is determined by considering the energy at which the systematic energy loss rate vanishes in the Fokker-Planck equation governing the evolution of $\langle nVF \rangle$ in a warm plasma, and that an accurate determination of the properties of the accelerated electron distribution can only be determined using the combination of X-ray spectroscopy and imaging outlined in detail in Kontar et al. (2019). We note, that while the expression (Eq. 28) is an approximation only, it does allow for a relatively robust statistical analysis (Aschwanden et al 2017), while the detailed fitting outlined in Kontar et al. (2019) is challenging for a large number of flare events. However, the detailed fitting procedure of Kontar et al. (2019), which constrains the plasma parameters T_e, n and L, is the recommended way to determine the nonthermal electron properties in an individual flare. Here, the use of Eq. (28) is likely to provide a lower limit of e_{th}, but is still useful for the purpose of a large statistical study.

From the low-energy cutoff approximation ε_{wt}, we can calculate the power in the electron flux P_{wt},

$$P_{wt}(\varepsilon \geq \varepsilon_{wt}) = \int_{\varepsilon_{wt}}^{\infty} f(\varepsilon) \, d\varepsilon = 4.3 \times 10^{24} \, b(\gamma) I_1 \left(\frac{\varepsilon_{wt}}{\epsilon_1} \right)^{-(\gamma-1)} \qquad [\text{erg s}^{-1}] \qquad (29)$$

and the total energy integrated over the flare duration is

$$E_{wt} = \int_{t_1}^{t_2} P_{wt}(\varepsilon \geq \varepsilon_{wt}, t) \, dt \qquad (30)$$

2.4. The Spectral Cross-Over Model

The bremsstrahlung spectrum $I(\varepsilon)$ of a thermal plasma with electron temperature T_e, as a function of the photon energy $\varepsilon = h\nu$ (with h the Planck constant and ν the frequency), setting the coronal electron density equal to the ion density ($n = n_i = n_e$), and neglecting factors of the order of unity (such as the Gaunt factor $g(\nu, T)$ in the approximation of the Bethe-Heitler bremsstrahlung cross-section), and the ion charge number, $Z \approx 1$, is (Brown 1974; Dulk and Dennis 1982),

$$I(\varepsilon) = I_0 \int \frac{\exp\left(-\varepsilon/k_B T\right)}{T^{1/2}} \frac{dEM(T)}{dT} \, dT \ , \qquad (31)$$

where $I_0 \approx 8.1 \times 10^{-39}$ keV cm^{-2} s^1 keV^{-1} and $dEM(T)/dT$ specifies the differential emission measure (DEM) $n^2 dV$ in the volume dV corresponding to a temperature range of dT,

$$\left(\frac{dEM(T)}{dT} \right) dT = n^2(T) \, dV \ . \qquad (32)$$

Regardless, whether we define this DEM distribution by an isothermal or by a multi-thermal plasma (Aschwanden 2007), the thermal spectrum $I(\varepsilon)$ falls off similarly to an exponential function at an energy of $\varepsilon \lesssim 20$ keV (or up to $\lesssim 40$) keV in extremal cases), while the nonthermal spectrum in the higher energy range of $\varepsilon \approx 20 - 100$ keV can be approximated by a single (or broken) power-law function (Eq. 3).

Because of the two different functional shapes, a cross-over energy ε_{co} can be defined by the change in the spectral slope between the thermal and the nonthermal spectral component. The electron energy spectrum, however, can have a substantially lower or higher cutoff energy (e.g., Holman 2003). We represent the combined spectrum with the sum of the (exponential-like) thermal and the (power-law-like) nonthermal component, i,e.,

$$I(\varepsilon) = I_{th}(\varepsilon) + I_{nth}(\varepsilon) = I_0 \int \frac{\exp\left(-\varepsilon/k_B T\right)}{T^{1/2}} \frac{dEM(T)}{dT} + I_1 \frac{(\gamma-1)}{\epsilon_1} \left(\frac{\epsilon_x}{\epsilon_1} \right)^{-\gamma} \ , \qquad (33)$$

where the cross-over energy ε_{co} can be determined in the (best-fit) model spectrum $I(\varepsilon)$ from the energy where the logarithmic slope is steepest, i.e., from the maximum of $\partial \log I(\varepsilon)/\partial \log \varepsilon$. The change of the spectral slope between the thermal and the nonthermal component is depicted in Fig. 2, where cross-over energies of $\varepsilon_{co} = 4.7$ keV for a small flare is calculated, and $\varepsilon_{co} = 19.5$ keV for a large flare.

From the low-energy cutoff ε_{co} we can calculate the power in the electron flux P_{co},

$$P_{co}(\varepsilon \geq \varepsilon_{co}) = \int_{\varepsilon_{co}}^{\infty} f(\varepsilon) \, d\varepsilon = 4.3 \times 10^{24} \, b(\gamma) I_1 \left(\frac{\varepsilon_{co}}{\epsilon_1} \right)^{-(\gamma-1)} \qquad [\text{erg s}^{-1}] \,, \tag{34}$$

and the total energy integrated over the flare duration is

$$E_{co} = \int_{t_1}^{t_2} P_{co}(\varepsilon \geq \varepsilon_{co}, t) \, dt \,. \tag{35}$$

We should be aware that the so determined cross-over energy ε_{co} is an upper limit only, and consequently the total energy E_{co} is a lower limit, unlike the other three low-energy cutoff models described in Sections 2.1-2.3.

3. OBSERVATIONS AND DATA ANALYSIS

The previously analyzed data set is based on all M and X-class flares observed with the *Atmospheric Imaging Assembly (AIA)* (Lemen et al. 2012) and the *Helioseismic and Magnetic Imager (HMI)* (Scherrer et al. 2012) onboard the *Solar Dynamics Observatory (SDO)* spacecraft (Pesnell et al. 2011) during 2010-2014, which amounts to 399 solar flare events. Here we use only those events that have been simultaneously observed with the *Ramaty High Energy Solar Spectroscopic Imager (RHESSI)* (Lin et al. 2002), which amount to 191 events, due to the duty cycle of $\approx 50\%$ of RHESSI when the orbit is on the sunward side.

3.1. Spectral Modeling of RHESSI Data

We use the same RHESSI data of 191 flare events as previously analyzed in Aschwanden et al. (2016), using the OSPEX (Object Spectral Executive) software (http://hesperia.gsfc.nasa.gov/). We re-analyzed the RHESSI data by optimizing the flare time intervals and the energy intervals (typically in the fitting range of $\varepsilon \approx 10 - 30$ keV) and obtained essentially the same results as described in Aschwanden et al. (2016). The observed hard X-ray photon spectrum has been fitted with an isothermal component (that is defined by the emission measure EM_{49} in units of 10^{49} [cm^{-3}] and the temperature T_e in units of [MK]), plus a nonthermal component with a broken power law function (that is defined by the nonthermal flux I_1 in units of [photons cm^{-2} s^{-1} keV^{-1}] at a reference energy of $\epsilon_1 = 50$ keV, and by the power law index δ of the fitted (lower) electron spectrum, which corresponds to a power law index of $\gamma = \delta - 1$ in the thick-target model. Examples of such two-component (thermal plus nonthermal) hard X-ray photon spectra are illustrated in Fig. 2. The hard X-ray spectra are fitted in time intervals of $\Delta t = 20$ s and yield the time-dependent best-fit parameters $EM_{49}(t)$, $T_e(t)$, $I_{nth}(t)$, and $\delta(t)$. The maximum values of the emission measure EM_{49}, the temperature T_e^{rhessi}, and the photon flux $I_1(t)$, during the flare duration τ_{flare}, as well as the minimum value of the spectral slope $\gamma = \delta - 1$, are listed in Table 2 for 160 (out of the 191) available events (omitting the less reliable cases with data gaps or inaccurate fits that result into outliers with extreme nonthermal energies of $E_{nth} > 10^{33}$ erg). More details of the spectral modeling of RHESSI data are given in Section 3.1 in Aschwanden et al. (2016).

3.2. Differential Emission Measure (DEM) Modeling

Besides the hard X-ray spectral modeling, we need also to measure the parameters of the spatial length scale L, the electron temperature T_e and the electron density n_e during the preflare phase as well as during the flare. The preflare electron density n_{e0} and the mean flare electron density n_e are listed in the three last columns of Table 2, i.e., labeled as $b_{10} = n_e^{bg}/10^{10}$ for the background and $n_{10} = n_e^{flare}/10^{10}$ during the flare.

The spatial length scale L has been deduced from measuring the flare area $A(t) = L(t)^2$, subject to corrections due to projection effects and electron density scale heights λ (Aschwanden et al. 2014, 2015), where the flare volume V is approximated by the Euclidean relationship,

$$V = L^3 . \tag{36}$$

From *differential emission measure (DEM)* modeling of the EUV data (observed with AIA) earlier (Aschwanden et al. 2015), we obtained the emission measure EM_{EUV} of the ("cold" and "warm") flare plasma and emission-measure-weighted temperature (T_{EUV}), and the corresponding electron density (n_{EUV}),

$$n_{EUV} = \sqrt{\frac{EM_{EUV}}{V}} , \tag{37}$$

measured at the peak time of the nonthermal hard X-ray flux.

In addition, the thermal emission measure (EM_R) and temperature T_R of the hot" flare plasma has been measured from the 2-component (thermal and nonthermal) spectral fit to the RHESSI data, but we should be aware that the RHESSI-inferred values are always biased towares the hottest temperature component. Nevertheless, the corresponding electron density n_R is then defined by the relationship during the flare at times t,

$$n_R(t) = \sqrt{\frac{EM_R(t)}{V}} . \tag{38}$$

Measuring the density at the starting time of the flare ($t = t_1$) yields then also an estimate of the preflare (or background) density (n_{bg}),

$$n_{bg} = n_R(t = t_1) = \sqrt{\frac{EM_R(t_1)}{V}} . \tag{39}$$

This preflare density n_{bg} is used in the electron number model (Section 2.1), where the maximum possible number of accelerated electrons in the full flare volume (essentially defined by the envelope volume of the entire flare arcade) during the preflare phase corresponds to the partial volume $V = L^3 q_{geo}$ (Eq. 6), with a geometric filling factor $q_{geo} = 1/4$ derived from the geometry of the diffusion region in a 3-D magnetic reconnection process with propagation of the hard X-ray footpoints along a flare ribbon with an approximative length L.

In the time-of-flight model (Section 2.2) we need an electron density n_e that is representative of the hot evaporating plasma, where electrons are stopped by collisional deflection. For this regime we use the emission measure $EM_R(t)$ and temperature $T_R(t)$ that is obtained from the spectral fitting of the thermal component observed with RHESSI.

In the warm target model (Section 2.3) we need an electron temperature that is characteristic for the "warm" target region (from the acceleration region to the top of the chromosphere), where the thermalization

of fast electrons takes place. We estimate this intermediate temperature from the geometric mean of the "warm" plasma observed in EUV (used in the DEM analysis) and the "hot" thermal plasma seen by RHESSI,

$$T_e(t_p) = [T_{EUV} \times T_R(t_p)]^{1/2} \ . \tag{40}$$

The temperature during the peak time t_p of the nonthermal hard X-ray flux is listed in Table 2, and a histogram is shown in Fig. (3a), which reveals a typical range of $T_e \approx 5 - 30$ MK.

3.3.   Statistical Results

The statistical distributions of the observables are shown in form of histograms on a linear or logarithmic scale in Fig. 3 and are listed in Table 1. The median values are: $T_e \approx 12.5$ MK for the maximum electron temperature (defined by the geometric mean between the EUV-inferred (T_{EUV}) and RHESSI-inferred (T_R) values); $\gamma \approx 7$ for the photon spectral index; $L \approx 10$ Mm for the spatial flare length scale; $\tau_{flare} \approx 0.5$ hrs for the flare duration (defined by the time difference between GOES start and peak times); $EM \approx 1 \times 10^{47}$ cm^{-3} for the emission measure observed by RHESSI; $F \approx 5 \times 10^{-4}$ [photons cm^{-2} s^{-1} keV^{-1}] for the photon flux at $\epsilon_1 = 50$ keV; $n_{eo} \approx 1 \times 10^{10}$ cm^{-3} for the preflare electron density; and $n_e \approx 2 \times 10^{10}$ cm^{-3} for the maximum flare electron density.

The statistical results of this analysis consist of the low-energy cutoffs ε_c and the total nonthermal energies E_{nth} of 191 M and X-class flares for all four theoretical models, which are tabulated in Fig. 3, while the size distribution of the low-energy cutoffs are displayed in Fig. 4, and the size distributions of nonthermal energies are shown in Fig. 5.

The size distributions of the low-energy cutoffs shown in Fig. 4 reveal almost identical median values for the first three models, $\varepsilon_{en} = 10.8$ keV for the electron number model (Fig. 4a), $\varepsilon_{tof} = 9.8$ keV for the time-of-flight model (Fig. 4b), and $\varepsilon_{wt} = 9.1$ keV for the warm target model (Fig. 4c), while the cross-over model reveals a value that is a factor of 2 higher, i.e., $\varepsilon = 21$ keV, which clearly corroborates the theoretical expectation that the spectral cross-over represents an upper limit on the low-energy cutoff only. Now we have a quantitative result that the low-energy cutoff is over-estimated by a factor of 2, statistically. This has the consequence that the nonthermal energy is underestimated by about a factor of about $2^4 = 16$ (for an electron power index of $\delta \approx 4$).

The size distributions of the nonthermal flare energies of the analyzed 191 flare events are displayed in Fig. 5, for each of the 4 low-energy cutoff models separately. The most conspicous difference between the different theoretical models is that the cross-over model is not able to produce nonthermal energies above $E_{nth} \gtrsim 2 \times 10^{30}$ erg, while the other three models all can produce energies up to $E_{nth} \lesssim 10^{33}$ erg. This is consistent with the expected bias that upper limits of the low-energy cutoff substantially underestimate the spectral integrated energy for the cross-over model, because the nonthermal energy scales with a very high nonlinear power (typically with a power index of $\delta \approx 4$). There are additional differences in the size distributions, especially regarding the power law index of the slope. The electron number model produces a negative power law slope of $\alpha \approx 1.4$, which is closest to most energy distributions of solar flares among the first three models shown in Fig. 5 (e.g., $\alpha_E = 1.53$; Crosby et al. 2013). The warm target model produces a surprisingly flat power law slope, with $\alpha \approx 1.1$, probably because of a systematic overestimation of the nonthermal energy of large flares. It is possible that the functional form of the low-energy cutoff spectrum, for which traditionally a step function at the lower boundary ε_c is assumed (e.g., Holman 2003), may be unrealistic. A smoother function for the boundary would steepen the power law slopes of the size

distributions for the warm target model and the time-of-flight model, and this way would bring them closer to the canonical value of $\alpha_E \approx 1.5$ observed in nonthermal energies (e.g., Crosby et al. 2013; see Table 3 in Aschwanden 2015).

3.4. Nonthermal Energy versus Dissipated Magnetic Energy

The main focus of this series of studies is the global energetics and energy partition in solar flares and *coronal mass ejections (CMEs)*. One of the previous results is that the nonthermal energy E_{th} as a fraction of the dissipated magnetic free energy E_{diss} is $q_E = E_{nth}/E_{diss} = 0.51 \pm 0.17$, so about half of the dissipated magnetic energy is converted into acceleration of electrons (Aschwanden et al. 2017). If we plot the same ratios for each of the theoretical models, we find $q_E^{ne} = 0.40 \pm 0.10$ for the electron number model (Fig. 6a), $q_E^{wt} = 0.45 \pm 0.10$ for the warm target model (Fig. 6b), $q_E^{tof} = 0.58 \pm 0.16$ for the time-of-flight model (Fig. 6c), and $q_E^{co} = 0.0034 \pm 0.0006$ for the cross-over model (Fig. 6d).

Since the three methods of calculating the nonthermal energy are essentially independent, we can improve the accuracy of the statistical means by averaging (logarithmically) the values from two or three models, which is shown in Fig. 7. Combining the electron number and the warm target model, we find $q_E^{ne,wt} = 0.57 \pm 0.10$ (Fig. 7a), combining the electron number and the time-of-flight method we find $q_E^{ne,tof} = 0.52 \pm 0.09$ (Fig. 7b), or by combining the warm target and the time-of-flight model we find $q_e^{wt,tof} = 0.61 \pm 0.10$ (Fig. 7c). The largest statistics is achieved by combining all three methods (excluding the cross-over model), for which we find $q_e^{en,wt,tof} = 0.57 \pm 0.08$ (Fig. 7d), which is perfectly consistent with the earlier result of $q_E = 0.51 \pm 0.17$ (Aschwanden et al. 2017). However, the new result has a smaller error of the mean ($q_{err} = \pm 0.07$) than the old result ($q_{err} = \pm 0.17$), thanks to the larger statistics with multiple independent methods, which cancel out some of the systematic errors of the various models. Note that the uncertainty of the ratio of the nonthermal to the dissipated magnetic energy, i.e., $q_E = E_{diss}/E_{magn}$, has been reduced to a factor of $\sigma \approx 5$ for a single flare event (Fig. 7d), while the error of the mean has been reduced to $q_{err} = 0.08$ (Fig. 7d).

4. DISCUSSION

4.1. Constraints for Low-Energy Cutoffs

We applied four different theoretical considerations in order to determine low-energy cutoffs in hard X-ray spectra, which are useful to pinpoint systematic errors of the models. Let us discuss which parameters constrain the various models, and whether the four models have some common physics.

In the electron number model (Section 2.1) we make the assumption that all electrons in the diffusion region of a magnetic reconnection volume are accelerated out of the thermal distribution, and therefore the flare volume $V = L^3$, the preflare electron density n_e, and the flare duration τ_{flare} are needed, as well as the observables that characterize the nonthermal spectrum $(I_1, \epsilon_1, \gamma)$. This method, therefore requires imaging observations (to measure the flare area $A = L^2$) and time profiles of the photon flux $F(t)$ (to measure the flare duration), while less physical parameters are required in the other models, and thus the electron number model provides the strongest constraints on the low-energy cutoff.

In the time-of-flight model (Section 2.2) we assume the equivalence between collisional deflection and electron time-of-flight times, which depend on the kinetic energy of electrons and the electron density, plus

the spatial scale of the electron time-of-flight distance L_{tof}. Hence imaging observations are required also, but the low-energy cutoff depends on L_{tof} and n_e only, which amounts to less constraints than the electron number model.

In the simplified approximation of the warm target model (Section 2.3), only the temperature T_e is required to characterize the collisional loss in the thick-target model (besides the spectral observable γ), which is based on the same physical process of collisional thermalization as the time-of-flight model, but requires less physical parameters.

Finally, in the spectral cross-over model (Section 2.4), the low-energy cutoff is directly estimated from the cross-over of the thermal and nonthermal spectrum, which does not require the knowledge of any physical parameter. However, this simplest method provides upper limits on the low-energy cutoff only.

So, the four methods are all complementary and at this point we cannot claim which model has a systematically higher value for the calculation of the low-energy cutoff, except for the fourth method that provides upper limits on the low-energy cutoff only. How compatible are the different models ? For the scaling of the physical parameters L and n_e in the two first models, we find $\varepsilon_{en} \propto (n_e L^3)^{-1/\gamma}$ for the electron number model (Eq. 9), and $\varepsilon_{tof} \propto (n_e L)^{1/2}$ for the time-of-flight model (Eq. 20), which is not directly compatible, and thus indicates incomplete physical models.

4.2. Functional Shape of Low-Energy Cutoff

In most previous, work the functional shape of the (nonthermal) electron injection spectrum is characterized with a power law function, i.e., $f(\varepsilon \geq \varepsilon_c) \propto \varepsilon^{-\delta}$, with a sharp cutoff at the low-energy side of the spectrum. This functional choice of the spectrum is not constrained by any physical model, but is simply chosen for mathematical convenience. The steep fall-off of this function at $\varepsilon \geq \varepsilon_c$ creates a particle energy distribution peaking near ε_c, which is unlikely to occur in a collisional plasma. We can use a kappa-distribution instead, already implemented in OSPEX. There are very few studies of the low-energy cutoff with smooth functions, such as modeling with kappa-distributions (Bian et al. 2014; Kontar et al. 2019).

Alternatively, we derived a smooth low-energy cutoff function in Appendix A, which is not based on a physical model either, but represents the simplest spectral function with a low-energy cutoff at the lower end and a power-law function at the upper end (Eq. A1). We show an example in Fig. 8, where the smooth low-energy cutoff function (according to Eq. A1) is shown with a minimum energy of $\varepsilon_c = 10.0$ keV, a power law slope of $\delta = 3$, and a peak energy of $\varepsilon_{peak} = \varepsilon_{min}(1 + 1/\delta) = 13.3$ keV. Although the difference of the sharp and the smooth electron injection spectrum does not appear to be paramount on a log-log scale (Fig. 8, left), the same functions rendered on a linear scale (Fig. 8, right) clearly show a significant difference in the electron flux. The suitability of a smooth cutoff function would require a spectral fit in the 10-30 keV range for this particular example. This example illustrates that the electron flux or the nonthermal energy calculated with a smooth cutoff function would yield a significantly different value than the sharp cutoff function. Smooth functions appear to be more realistic in a collisional plasma than an infinitely sharp edge at the low-energy cutoff.

4.3. Uncertainties of Nonthermal Energies in Flares

A central question of this study is the statistical uncertainty of the various forms of flare energies, in particular the nonthermal energies of flares. From the distributions of (logarithmic) nonthermal energies we found means and standard deviations of $q_E = 0.40 \pm 0.10$ for the electron number model (Fig. 6a), $q_E = 0.58 \pm 0.16$ for the time-of-flight model (Fig. 6c), and $q_E = 0.45 \pm 0.19$ for the warm target model (Fig. 6b), which are fully compatible with the previously measured values of $q_E = 0.51 \pm 0.17$ based on the warm target model by using different temperature mixtures (Aschwanden et al. 2017). The error of the mean is even smaller when all measurements from the three methods are combined, i.e., $q_e = 0.57 \pm 0.08$ (Fig. 7d). However, the standard deviations of the energy ratios scatter by factors of $\sigma \approx 8 - 24$ (Fig. 6), which represents the uncertainties for single events. Combining the first three methods, the uncertainty for a single event comes down to a factor of $\sigma = 5.4$ (Fig. 7d). Since these energy ratios $q_E = E_{nth}/E_{diss}$ involve both the nonthermal energies and the dissipated magnetic energies, the uncertainties of both types of energies are folded into these uncertainties. In summary, we can say that the statistical error of the mean nonthermal-to-magnetic energy ratio has been reduced to $\gtrsim 8\%$, while the uncertainty of the ratio for an individual event has been reduced to a factor of 5. Future studies should concentrate on cases with unphysical values, such as flares that yield nonthermal energies that are larger than the dissipated magnetic energy.

5. CONCLUSIONS

In this study we revisit the nonthermal flare energies, previously calculated for 191 flare events (of M and X-class) observed with RHESSI during the time period of 2010-2014 (Aschwanden et al. 2016), based on the warm target model of Kontar et al. (2015, 2019). The warm target model predicts a low-energy cutoff that scales linearly with the temperature T_e of the warm target and the spectral power-law slope δ of the nonthermal electron flux, i.e., $\varepsilon_c \approx \delta k_B T_e$ (Kontar et al. 2015). The power-law slope δ is obtained from a spectral fit of RHESSI data with the OSPEX software, applied to the nonthermal energy range of $\varepsilon \approx 10 - 30$ keV. The temperature is weighted by a mixture of preflare plasma temperatures (T_{cold}) and heated upflowing evaporating flare plasma temperatures (T_{hot}), which has a mean value of $T_e = 8.8 \pm 6.0$ MK for AIA data, from which the mean values of the differential emission measure (DEM) peak temperatures were used in the previous study (Aschwanden et al. 2016). These parameters yielded a mean energy cutoff of $e_{wt} = 6.2 \pm 1.6$ keV in the warm target model, and an energy fraction of $q_E = 0.51 \pm 0.17$ for the mean (logarithmic) ratio of the nonthermal energy to the dissipated magnetic energy.

Since the nonthermal flare energies represent the largest fraction of the total energy budget in flares, and since the determination of the nonthermal flare energy has the largest uncertainty due to the unknown low-energy cutoff, we decided to revisit the calculation of nonthermal energies with four different physical models that complement each other, which we summarize in the following.

1. The *electron number model* estimates the number of electrons (in the preflare phase) that can be accelerated in a flaring region, which is the product of the (preflare) electron density n_e, the flare volume V, and the flare duration τ_{flare}. Some geometry factor is required to relate the acceleration volume to the flaring volume seen in EUV. Setting this total electron number equal to the total number of electrons contained in the electron injection spectrum according to the thick-target model, a low-energy cutoff ε_{en} can be derived that depends on the spectral parameters $[I_1(t), \gamma(t)]$ and the physical parameters $[n_e, V, \tau_{flare}]$. Using this model we infer a low-energy cutoff of $\varepsilon_{en} = 10.8 \pm 7.5$ keV and a

value of $E_{nth}/E_{diss} = 0.40 \pm 0.10$ for the ratio of the nonthermal to the dissipated magnetic energy.

2. The *time-of-flight* model assumes the equivalence of the collisional deflection time t_{defl} and the electron time-of-flight time scale t_{tof}. This model essentially assumes a non-collisional plasma for $t_{tof} < t_{defl}$, and a collisional plasma for longer propagation times, $t_{tof} > t_{defl}$. This model predicts a low-energy cutoff that depends on the electron time-of-flight distance L_{tof} (which we approximate with the length scale L_{tof} of the flare area) and the preflare electron density n_e. Using this model we infer a low-energy cutoff of $\varepsilon_{tof} = 9.8 \pm 9.5$ keV and a value of $E_{nth}/E_{diss} = 0.58 \pm 0.16$ for the ratio of the nonthermal to the dissipated magnetic energy.

3. The *warm target* model, derived by Kontar et al. (2015, 2016), replaces the original cold thick-target model, where in addition to the "cold" chromospheric plasma, a "warm" coronal plasma is added, where the precipitating electrons collisionally thermalize in the ambient coronal Maxwellian distribution. Importantly, the thermalized electrons contribute to the overall thermal spectrum. The "warm" temperature of the coronal plasma can be a mixture of cold and hot plasma, which we approximate here with the geometric mean of the "cold" EUV temperature (obtained from DEM modeling) and the "hot" soft X-ray plasma temperature (obtained from RHESSI fitting with a combined thermal plus nonthermal spectrum). Using this model we infer a low-energy cutoff of $\varepsilon_{wt} = 9.9 \pm 4.8$ keV and a value of $E_{nth}/E_{diss} = 0.45 \pm 0.10$ for the ratio of the nonthermal to the dissipated magnetic energy.

4. The *spectral cross-over* model is included here for comparison. An upper limit for the low-energy cutoff can be found from the intersection point of the thermal (low-energy) component and the nonthermal (high-energy) component in spectral fits of RHESSI data, using the OSPEX software. As it was established earlier, the low-energy cutoff is different by about a factor of two, for which we find a range of $\varepsilon_{co} = 21.3 \pm 5.8$ keV.

In summary, we conclude that the first three models yield consistent values for the low-energy cutoff in the order of $\varepsilon \approx 10$ keV, while the spectral cross-over model yields upper limits only, at $\varepsilon \approx 21$ keV. It is interesting that the first three different models with different assumptions lead to similar results. Combining all three methods, we find a mean energy partition of $q_E = 0.57 \pm 0.08$ for nonthermal energies, while the uncertainty in a single event has been reduced to a factor of 5.

<div align="center">

APPENDIX A: Smooth Low-Energy Cutoff Function

</div>

The electron injection spectrum in the thick-target model is generally rendered with a power-law function that drops off steeply above the cutoff energy at $\varepsilon \geq \varepsilon_c$, and is set to zero below this cutoff energy at $\varepsilon < \varepsilon_c$ (e.g., Holman 2003). This form of a spectral function results into an extremely narrow function in energy that is almost mono-energetic. For collisional processes, a sharp cutoff function may be unrealistic, while a smooth cutoff function is more likely to occur. We define a smooth electron injection function $f_e(\varepsilon)$ simply by introducing a multiplicative term $(1 - \varepsilon_c/\varepsilon)$,

$$f_e^{sm}(\varepsilon) = f_e(\varepsilon)\left(1 - \frac{\varepsilon_{min}}{\varepsilon}\right) \ , \qquad (A1)$$

which fulfills the two constraints of a low-energy cutoff of $f_e^{sm}(\varepsilon = \varepsilon_{min}) = 0$ and the approximative form of a power-law-like function at higher energies, i.e., at $\varepsilon \gtrsim \varepsilon_{min}$.

The smooth electron injection spectrum (as shown with thick linestyle in Fig. 8) has then the functional form of (based on Eq. 2),

$$f_e^{sm}(\varepsilon) = f_1 \left(\frac{\varepsilon}{\varepsilon_{min}} \right)^{-\delta} \left(1 - \frac{\varepsilon_{min}}{\varepsilon} \right) \ . \tag{A2}$$

The smoothed electron injection function has a minimum energy of ε_{min}, and a peak at ε_{peak}. If we set the peak energy equal to the sharp cutoff, i.e., $\varepsilon_{peak} = \varepsilon_c$, which can be calculated from the derivative $\partial f_e^{sm}(\varepsilon)/\partial \varepsilon = 0$, we obtain

$$\varepsilon_{peak} = \varepsilon_{min} \left(1 + \frac{1}{\delta} \right) \ . \tag{A3}$$

For instance, for the example shown in Fig. 8, the energy ratio is $\varepsilon_{peak} = \varepsilon_{min}(1 + 1/\delta) = 4/3 = 1.333$ for $\delta = 3$. For steeper slopes δ the ratio becomes smaller, such as $\varepsilon_{peak} = \varepsilon_{min}(1 + 1/\delta) = 9/8 = 1.125$ for $\delta = 8$.

We can now analytically calculate the functional form of the total number of electrons above a cutoff energy of ε_c,

$$F^{sm}(\varepsilon \geq \varepsilon_{min}) = \int_{\varepsilon_{min}}^{\infty} f_e(\varepsilon) \ \left(1 - \frac{\varepsilon_c}{\varepsilon} \right) d\varepsilon = F(\varepsilon \geq \varepsilon_c) \left(\frac{1}{1+\gamma} \right) \qquad [\text{electrons s}^{-1}] \ , \tag{A4}$$

where the integration of $F(\varepsilon \geq \varepsilon_c)$ produces a simple multiplication factor $1/(1+\gamma)$ that depends on the spectral slope γ of the photon spectrum only.

Similarly, we can analytically calculate the power $F^{sm}(\varepsilon \geq \varepsilon_c)$ in nonthermal electrons above this cutoff energy,

$$P^{sm}(\varepsilon \geq \varepsilon_{min}) = \int_{\varepsilon_c}^{\infty} f_e(\varepsilon) \ \varepsilon \ \left(1 - \frac{\varepsilon_c}{\varepsilon} \right) d\varepsilon = P(\varepsilon \geq \varepsilon_c) \frac{1}{\gamma} \qquad [\text{erg s}^{-1}] \ , \tag{A5}$$

where the integration of $P(\varepsilon \geq \varepsilon_c)$ produces a similar multiplication factor $(1/\gamma)$ that depends on the spectral slope γ of the photon spectrum only. Since the correction of the sharply peaked electron injection function by a smoothed function depends on the power law slope γ, we expect a change in the energy-dependence of the distribution functions.

The smooth definition of the electron injection function affects also the value of the low-energy cutoff for the electron number model, since the total number of electrons N_e (Eq. 6) changes as,

$$N_e = F(\varepsilon \geq \varepsilon_c) \left(\frac{1}{1+\gamma} \right) \tau_{flare} \qquad [\text{electrons}] \ , \tag{A6}$$

and the resulting low-energy cutoff is modified by the factor $1/(1+\gamma)$, compared with Eq. (9), i.e.,

$$\varepsilon_{en} = \epsilon_1 \left[\frac{n_{e0} \ L_{10}^3 \ q_{geo} \ \epsilon_1}{0.72 \ \gamma^2(\gamma^2 - 1) \ I_1 \ \tau_{flare}} \right]^{-1/\gamma} \qquad [\text{keV}] \ . \tag{A7}$$

Thus, the smooth electron injection function causes this modification in the calculation of the low-energy cutoff of the electron number model, but it does not affect the time-of-flight model (Eq. 20), the warm target model (Eq. 28), or the cross-over model (Eq. 33), since these other models do not directly depend on the chosen electron injection function. Future studies may fit the smoothed electron injection function (Eq. A1) in order to obtain a more accurate estimate of flare energies.

APPENDIX B: Parameter Dependence of Low-Energy Cutoff

B1 : The Electron Number Model

The input parameters of our low-energy cutoff models affect the final result of the low-energy cutoff value ε in a specific way for each parameter. In Table 1 (based on the parameter distributions shown in Fig. 3) we list the mean and standard deviations $x_{mean} \pm \sigma$ of each observed variable ($x = T_e, \gamma, L, \tau_{flare}, EM, I_1, n_e, n_{e0}$), which can be characterized by the variance ratio σ/x_{mean}, found to range from $\sigma_\gamma/\gamma = 1.20$ (for spectral slopes) up to a factor of $\sigma_{EM}/EM = 11.0$ (for emission measures) (Table 1).

We investigate now how these typical parameter variations affect the typical values of the resulting low-energy cutoffs ε. We start with the electron number model (Eq. 9),

$$\varepsilon_{en} = \epsilon_1 \left[\frac{n_{e0} \; L_{10}^3 \; q_{geo} \; \epsilon_1}{0.72 \; \gamma^2(\gamma - 1) \; I_1 \; \tau_{flare}} \right]^{-1/\gamma} \qquad [\text{keV}] \; . \qquad (B1)$$

Denoting the mean value of the preflare electron density with n_{e0} and the value of a standard deviation higher with $\tilde{n}_{e0}$ (with $[\tilde{n}_{e0}/n_{e0}] = 6.34$ according to Table 1), the corresponding low-energy cutoff value $\tilde{\varepsilon}_{en}$ is

$$\frac{\tilde{\varepsilon}_{en}}{\varepsilon_{en}} = \left[\frac{\tilde{n}_{e0}}{n_{e0}} \right]^{-1/\gamma} = [6.34]^{-1/7} = 0.77 \; , \qquad (B2)$$

which means that the low-energy cutoff value $\tilde{\varepsilon}_{en}$ comes out to be 23% lower for a preflare electron density that is a standard deviation higher than the mean value. This value can be considered as an upper limit of the uncertainty of the low-energy cutoff value, if all the variance in the electron density measurements are due to measurement errors in the electron density. Practically, since the obtained mean value is $\varepsilon_{en} = 10.8 \pm 7.5$ keV (Fig. 4a), this uncertainty is 0.23×10.8 keV ≈ 2.5 keV.

Next we investigate the uncertainty caused by the nonthermal flux I_1. Denoting the mean value of the nonthermal flux I_1 and the value of a standard deviation higher with $\tilde{I}_1$ (with $[\tilde{I}_1/I_1] = 6.40$ according to Table 1), the corresponding low-energy cutoff value $\tilde{\varepsilon}_{en}$ is

$$\frac{\tilde{\varepsilon}_{en}}{\varepsilon_{en}} = \left[\frac{I_1}{\tilde{I}_1} \right]^{-1/\gamma} = [1./6.40]^{-1/7} = 1.30 \; , \qquad (B3)$$

which means that the low-energy cutoff value $\tilde{\varepsilon}_{en}$ comes out to be 30% higher for a nonthermal flux that is a standard deviation higher than the mean value. This value indicates an uncertainty of 0.30×10.8 keV ≈ 3.2 keV, which is an upper limit of the uncertainty, if all variance is due to measurement errors of the nonthermal flux.

Next we investigate the uncertainty due to the flare duration τ_{flare}. Denoting the mean value of the flare duration τ_{flare} and the value of a standard deviation higher with $\tilde{\tau}_{flare}$ (with $[\tilde{\tau}_{flare}/\tau_{flare}] = 1.84$ according to Table 1), the corresponding low-energy cutoff value $\tilde{\varepsilon}_{en}$ is

$$\frac{\tilde{\varepsilon}_{en}}{\varepsilon_{en}} = \left[\frac{\tau_{flare}}{\tilde{\tau}_{flare}} \right]^{-1/\gamma} = \left[\frac{1}{1.84} \right]^{-1/7} = 1.15 \; , \qquad (B4)$$

which means that the low-energy cutoff value $\tilde{\varepsilon}_{en}$ comes out to be 15% higher for a flare duration that is a standard deviation higher than the mean value. This value indicates an uncertainty of 0.15×10.8 keV ≈ 1.6 keV, which is an upper limit of the uncertainty, if all variance is due to measurement errors of the flare duration.

Next we investigate the uncertainty due to the flare length scale L. Denoting the mean value of the length scale L and the value of a standard deviation higher with $\tilde{L}$ (with $[\tilde{L}/L] = 1.55$ according to Table 1), the corresponding low-energy cutoff value $\tilde{\varepsilon}_{en}$ is

$$\frac{\tilde{\varepsilon}_{en}}{\varepsilon_{en}} = \left[\frac{\tilde{L}^3}{L^3}\right]^{-1/\gamma} = \left[1.55^3\right]^{-1/7} = 0.83 \; , \tag{B5}$$

which means that the low-energy cutoff value $\tilde{\varepsilon}_{en}$ comes out to be 17% lower for a length scale that is a standard deviation larger than the mean value. This value indicates an uncertainty of 0.17×10.8 keV $\approx$ 1.8 keV, which is an upper limit of the uncertainty, if all variance is due to measurement errors of the flare length scale.

Next we investigate the uncertainty due to the spectral slope γ. Denoting the mean value of the spectral slope γ and the value of a standard deviation higher with $\tilde{\gamma}$ (with $[\tilde{\gamma}/\gamma] = 1.20$ according to Table 1), the corresponding low-energy cutoff value $\tilde{\varepsilon}_{en}$ is

$$\frac{\tilde{\varepsilon}_{en}}{\varepsilon_{en}} = \left[\frac{\gamma^2(\gamma - 1)}{\tilde{\gamma}^2(\tilde{\gamma} - 1)}\right]^{-1/\gamma} = [1.63]^{-1/7} = 0.93 \; , \tag{B6}$$

which means that the low-energy cutoff value $\tilde{\varepsilon}_{en}$ comes out to be 7% lower for a spectral index scale that is a standard deviation larger than the mean value. This value indicates an uncertainty of 0.07×10.8 keV ≈ 0.8 keV, which is an upper limit of the uncertainty, if all variance is due to measurement errors of the spectral slope.

Finally, we investigate also the uncertainty due to the geometric parameter $q_{geo} = 1/4$, which is assumed for the ratio of the flare arcade volume with respect to an encompassing cube. Denoting the mean value of the geometry factor with q_{geo} and the value of a factor two higher with $\tilde{q}_{geo}$ (i.e., $[\tilde{\gamma}/\gamma] = 2$), the corresponding low-energy cutoff value $\tilde{\varepsilon}_{en}$ is

$$\frac{\tilde{\varepsilon}_{en}}{\varepsilon_{en}} = \left[\frac{\tilde{q}_{geo}}{q_{geo}}\right]^{-1/\gamma} = [2]^{-1/7} = 0.91 \; , \tag{B7}$$

which means that the low-energy cutoff value $\tilde{\varepsilon}_{en}$ comes out to be 9% lower for a geometry factor that is a factor two larger than the mean value. This value indicates an uncertainty of 0.09×10.8 keV ≈ 1.0 keV, which is an upper limit on the uncertainty of the geometry factor.

In summary, upper limits of the uncertainties σ_x of the low-energy cutoff ε_{en} in our electron number model are estimated (in decreasing order) from the following parameters: the nonthermal flux I_1 (i.e., $\sigma_{I1} <$ 30% of the low-energy cutoff value),) preflare electron density $n_{e0}(< 23\%)$, flare length scale $\tau_{flare}(< 17\%)$, flare duration $\tau_{flare}(< 15\%)$, geometric model $q_{geo}(< 9\%)$, and spectral index $\gamma(< 7\%)$. In these estimates we make the assumption that the variance of the values is entirely caused by measurement errors, which constitutes upper limits on the uncertainties of the low-energy cutoff values.

B2 : The Time-of-Flight Model

We proceed now to our second model, the so-called time-of-flight model, which depends on two parameters only, the length scale L and the mean electron density n_e during flares (Eq. 20),

$$e_{tof} \approx 28 \left(\frac{L}{10^{10} \text{ cm}}\right)^{1/2} \left(\frac{n_e}{10^{10} \text{ cm}^{-3}}\right)^{1/2} \qquad [\text{keV}] \; . \tag{B8}$$

Similarly to the previous method, we investigate the uncertainty due to the length scale L. Denoting the mean value of the length scale L and the value of a standard deviation higher with $\tilde{L}$ (with $[\tilde{L}/L] = 1.55$ according to Table 1), the corresponding low-energy cutoff value $\tilde{\varepsilon}_{en}$ is

$$\frac{\tilde{\varepsilon}_{en}}{\varepsilon_{en}} = \left[\frac{\tilde{L}}{L}\right]^{1/2} = [1.55]^{1/2} = 1.24 \ , \tag{B9}$$

which means that the low-energy cutoff value $\tilde{\varepsilon}_{en}$ comes out to be 24% higher for a length scale that is a standard deviation larger than the mean value. Using the distribution shown in Fig. 4b, i.e., $\varepsilon_{tof} = 9.8 \pm 9.5$ keV. This value indicates a mean uncertainty of 0.24×9.8 keV ≈ 2.4 keV, which is an upper limit of the uncertainty, when all variance is due to measurement errors of the length scale.

Denoting the mean value of the flare electron density with n_e and the value of a standard deviation higher with $\tilde{n}_e$ (with $[\tilde{n}_e/n_e] = 3.69$ according to Table 1), the corresponding low-energy cutoff value $\tilde{\varepsilon}_{en}$ is

$$\frac{\tilde{\varepsilon}_{en}}{\varepsilon_{en}} = \left[\frac{\tilde{n}_e}{n_e}\right]^{1/2} = [3.69]^{1/2} = 1.92 \ , \tag{B10}$$

which means that the low-energy cutoff value $\tilde{\varepsilon}_{en}$ comes out to be 92% higher for a flare electron density that is a standard deviation higher than the mean value. This value can be considered as an upper limit of the uncertainty of the low-energy cutoff value, if all the variance in the electron density measurements are due to measurement errors in the electron density. Practically, since the obtained mean value is $\varepsilon_{en} = 9.8 \pm 9.5$ keV (Fig. 4b), this uncertainty is 0.92×10.8 keV ≈ 9.0 keV. This large uncertainty implies a high sensitivity of the low-energy cutoff on the flare density, while it substantially less sensitive to the flare length scale. It is therefore imperative to measure the flare density accurately, which requires detailed DEM analysis.

B3 : The Warm Target Model

Finally, we investigate the parameter dependence of the warm target model, which in its simplest form (Eq. 28),

$$\varepsilon_{wt} \approx (\xi + 2)k_B T_e = \delta \ k_B T_e \ = (\gamma + 1)k_B T_e, \tag{B12}$$

where $\xi = \gamma - 1$ is the power-law slope of the source-integrated mean electron flux spectrum (see Eqs. (8)-(10) in Kontar et al. 2015), and T_e is the temperature of the warm target plasma. Denoting the mean value of the spectral index with γ and the value of a standard deviation higher with $\tilde{\gamma}$ (with $[\tilde{\gamma}/\gamma] = 1.20$ according to Table 1), the corresponding low-energy cutoff value $\tilde{\varepsilon}_{en}$ is

$$\frac{\tilde{\varepsilon}_{en}}{\varepsilon_{en}} = \left[\frac{\tilde{\gamma} + 1}{\gamma + 1}\right] = 1.18 \tag{B13}$$

which means that the low-energy cutoff value $\tilde{\varepsilon}_{en}$ comes out to be 18% higher for a spectral index that is a standard deviation higher than the mean value. This value can be considered as an upper limit of the uncertainty of the low-energy cutoff value, if all the variance in the spectral index measurements are due to measurement errors in the electron density. Practically, since the obtained mean value is $\varepsilon_{en} = 9.9 \pm 4.8$ keV (Fig. 4c), this uncertainty is 0.18×9.9 keV ≈ 2.0 keV.

The temperature dependence can be calculated by denoting the mean value of the spectral index with T_e and the value of a standard deviation higher with $\tilde{T}_e$ (with $[\tilde{T}_e/T_e] = 1.40$ according to Table 1), the

corresponding low-energy cutoff value $\tilde{\varepsilon}_{en}$ is

$$\frac{\tilde{\varepsilon}_{en}}{\varepsilon_{en}} = \left[\frac{\tilde{T}_e}{T_e}\right] = 1.40 \qquad (B14)$$

which means that the low-energy cutoff value $\tilde{\varepsilon}_{en}$ comes out to be 40% higher for a spectral index that is a standard deviation higher than the mean value. This value can be considered as an upper limit of the uncertainty of the low-energy cutoff value, if all the variance in the spectral index measurements are due to measurement errors in the electron density. Practically, since the obtained mean value is $\varepsilon_{en} = 9.9 \pm 4.8$ keV (Fig. 4c), this uncertainty is 0.40×9.9 keV ≈ 4.0 keV.

Thus, for the warm target model, uncertainties up to 18% of the low-energy cutoff could be arise due to uncertainties in the spectral index, and uncertainties up to 40% of the low-energy cutoff could be caused by uncertainties of the temperature measurement.

References

Aschwanden, M.J.: 2004, *Physics of the Solar Corona. An Introduction*, Berlin: Springer and Praxis, p.216.

Aschwanden, M.J. 2007, ApJ 661, 1242.

Aschwanden, M.J., Xu, Y., and Jing, J. 2014, ApJ 797, 50. *Global energetics of solar flares: I. Magnetic Energies*

Aschwanden, M.J. 2015, ApJ 814, 19.

Aschwanden, M.J., Boerner, P., Ryan, D., Caspi, A., McTiernan, J.M., and Warren, H.P., 2015, ApJ 802, 53. *Global energetics of solar flares: II. Thermal Energies*

Aschwanden, M.J., O'Flannagain, A., Caspi, A., McTiernan, J.M., Holman, G., Schwartz, R.A., and Kontar, E.P. 2016, ApJ 832, 27. *Global energetics of solar flares: III. Nonthermal Energies*

Aschwanden, M.J. 2016, ApJ 831, 105. *Global energetics of solar flares. IV. Coronal mass ejection energetics*

Aschwanden, M.J., Caspi, A., Cohen, C.M.S., Holman, G.D., Jing, J., Kretzschmar, M., Kontar, E.P., McTiernan, J.M., O'Flannagain, A., Richardson, I.G., Ryan, D., Warren, H.P., and Xu,Y. 2017, ApJ 836, 17. *Global energetics of solar flares: V. Energy closure*

Aschwanden, M.J. 2017, ApJ 847, 27. *Global energetics of solar flares. VI. Refined energetics of coronal mass ejections.*

Aschwanden, M.J. and Gopalswamy, N. 2019, ApJ (in press). *Global energetics of solar flares. VII. The aerodynamic drag in coronal mass ejections.*

Aschwanden, M.J. 2019, *New Millennium Solar Physics*, Astrophysics and Space Science Library Vol. 458, ISBN 978-3-030-13954-4; New York: Springer.

Aschwanden, M.J. 2019, *New Millennium Solar Physics*, Section 11.8, New York: Springer, (in press), http://www.lmsal.com/∼aschwand/bookmarks_books2.html.

Benz, A.O. 1993, *Plasma Astrophysics. Kinetic processes in solar and stellar coronae*, Kluwer Academic Publishers: Dordrecht, p.45.

Bian, N.H., Emslie, A.G., Stackhouse, D.J., and Kontar, E.P. 2014, ApJ 796, 142.

Brown, J.C. 1971, SoPh 18, 489.

Brown, J.C. 1974, in Proc. Symp. IAU COll. 57, *Coronal disturbances*, (e.d., G.J. Newkirk, Jr. (Dordrecht: Reidel), 523.

Carmichael, H. 1964, in *The Physics of Solar Flares*, Proc. AAS-NASA Symposium, (ed. W.N. Hess), NASA-SP 50, NASA Science and Technical Information Division, Washington DC p.451.

Crosby, N.M., Aschwanden, M.J., and Dennis, B. 1993, SoPh 143, 275.

Culhane, J.L. 1969, MNRAS 144, 375.

Culhane, J.L. and Acton, L. 1970, MNRAS 151, 141.

Dennis, B.R. 1985, SoPh 100, 465.

Dulk, G.A. and Dennis, B.R. 1982, ApJ 260, 875.

Galloway, R.K., MacKinnon, A.L., Kontar, E.P. and Helander P. 2005, A&A 438, 1107.

Goncharov, P.R., KJuteev, B.V., Ozaki, T., and Sudo, S. 2010, PhPl 17, 112313.

Guo, J., Emslie, A.G., Kontar, E.P., et al. 2012a, A&A 543, A53.

Guo, J., Emslie, A.G., Massone, A.M., Piana, M., and PIana, M. 2012b, ApJ 755, 32.

Guo, J., Emslie, A.G., and Piana, M. 2013, ApJ 766, 28.

Hirayama, T. 1974, SoPh 34, 323.

Holman, G.D. 2003, ApJ 586, 606.

Holman, G.D., Aschwanden, M.J., Aurass, M.J. et al. 2011, SSRv 159, 107.

Ireland, J., Tolbert, A.K., Schwartz, R.A., Holman, G.D., and Dennis, B.R. 2013, ApJ 769, 89.

Jeffrey, N.L.S., Kontar, E.P., Bian, N.H., and Emslie, A.G. 2014, ApJ 787, 86.

Jeffrey, N.L.S., Kontar, E.P., and Emslie, A.G. 2015, A&A 584, 89.

Kontar, E.P., Jeffrey, N.L.S., Emslie, A.G., and Bian, N.H. 2015, ApJ 809, 35.

Kontar, E.P., Jeffrey, N.L.S., and Emslie, A.G. 2019, ApJ 871, 225.

Kopp, G. and Pneuman, G.W. 1976, SoPh 50, 85.

Lemen,J.R., Title, A.M., Akin,D. J., Boerner, P.F., Chou, C., Drake, J.F., Duncan, D.W., Edwards, C.G., et al. 2012, SoPh 275, 17.

Lin, R.P., Dennis,B.R., Hurford,G.J., Smith,D.M., Zehnder,A., Harvey,P.R., Curtis,D.W., et al. 2002, Solar Phys. 210, 3.

Pesnell, W.D., Thompson, B.J., and Chamberlin, P.C. 2011, SoPh 275, 3.

Petrosian, V. 2000, SSRv 173, 535.

Scherrer, P.H., Schou, J., Bush, R. I., Kosovichev, A.G., Bogart, R.S., Hoeksema, J T., Liu, Y., Duvall, T.L., et al. 2012, SoPh 275, 207.

Somov, B.V. 2000, *Cosmic Plasma Physics*, Dordrecht: Kluwer Academic Publishers.

Sturrock, P.A. 1966, Nature 5050, 695.

Table 1: The ranges (x_{min}, x_{max}), medians (x_{med}), means and standard deviations $x_{mean} \pm \sigma$, and variance ratios (σ/x_{mean}) of the observed variables in the determination of the low-energy cutoff ε_c are listed according to Fig. 2, for a total of 191 M and X-class flares.

Parameter	Minimum	Median	Maximum	Mean std	Variance ratio
	x_{min}	x_{med}	x_{max}	$x_{mean} \pm \sigma$	σ/x_{mean}
Temperature T_e (MK)	3.4	12.5	33.7	13.5±5.4	1.40
Spectral slope γ	2.8	7.2	10.4	7.0±1.4	1.20
Length scale L (Mm)	1.7	9.8	34.8	10.9±6.0	1.55
Flare duration t_{flare} (s)	$10^{2.20}$	$10^{3.22}$	$10^{3.98}$	$10^{3.2\pm0.27}$	1.84
Emission measure EM (cm^{-3})	$10^{44.3}$	$10^{47.0}$	$10^{51.4}$	$10^{47.1\pm1.04}$	11.0
Photon flux I_1 (photons cm^{-2} s^{-1} keV^{-1})	$10^{-5.12}$	$10^{-3.34}$	$10^{-0.65}$	$10^{-3.27\pm0.81}$	6.40
Flare electron density n_e	$10^{8.30}$	$10^{9.97}$	$10^{12.13}$	$10^{10.1\pm0.80}$	3.69
Preflare electron density n_{e0}	$10^{8.00}$	$10^{9.34}$	$10^{13.41}$	$10^{9.60\pm0.80}$	6.34

Table 2.   Observables of flare hard X-ray emission in 143 M and X-class flare events.

ID	Date	Time	GOES class	Heliogr. position	Dur. flare τ_{flare} (s)	Emission measure EM_{49} (cm^{-3})	Temp. max. T_e (MK)	Photon flux I_1 (cm^2 s keV^{-1})	Spectral slope γ	Length scale L (Mm)	Density maximum n_{10} (cm^{-3})	Density preflare b_{10} (cm^{-3})
1	20100612	0030	M2.0	N23W47	904	0.00428	10.73	0.0000736	4.24	13.23	0.43	0.18
2	20100613	0530	M1.0	S24W82	1852	0.00002	12.67	0.0000181	5.04	12.25	0.03	0.01
3	20100807	1755	M1.0	N13E34	3700	0.00005	12.03	0.0007735	4.09	25.10	0.02	1.64
4	20101016	1907	M2.9	S18W26	1572	0.03886	18.18	0.0004585	8.06	15.13	1.06	0.08
10	20110213	1728	M6.6	S21E04	2324	0.01753	19.21	0.0088956	7.10	15.94	0.66	0.03
12	20110215	0144	X2.2	S21W12	2628	0.24398	21.25	0.0443819	7.06	28.41	1.03	0.13
13	20110216	0132	M1.0	S22W27	1368	0.00240	18.71	0.0007753	6.83	12.16	0.37	0.14
15	20110216	1419	M1.6	S23W33	1692	0.01667	12.12	0.0003076	7.54	10.74	1.16	0.33
16	20110218	0955	M6.6	S21W55	1780	0.09996	9.70	0.0083943	7.21	10.61	2.89	0.15
18	20110218	1259	M1.4	S20W70	1944	0.01476	13.66	0.0006862	7.13	6.44	2.35	0.60
19	20110218	1400	M1.0	N17E04	1264	0.01366	6.92	0.0002906	4.33	9.43	1.28	0.21
20	20110218	2056	M1.3	N15E00	884	0.01607	7.51	0.0001562	7.99	8.43	1.64	0.13
21	20110224	0723	M3.5	N14E87	3332	0.01042	10.86	0.0000111	9.23	20.02	0.36	0.06
22	20110228	1238	M1.1	N22E35	732	0.00133	8.45	0.0013909	6.51	10.20	0.35	0.26
23	20110307	0500	M1.2	N23W47	1340	0.00166	8.11	0.0004404	7.35	5.98	0.88	0.88
28	20110307	1943	M3.7	N30W48	3196	0.00172	10.61	0.0029535	5.13	26.55	0.10	0.03
29	20110307	2145	M1.5	S17W82	1232	0.00071	10.31	0.0023961	5.78	5.73	0.61	0.04
30	20110308	0224	M1.3	S18W80	1460	0.01306	4.13	0.0008550	6.69	9.31	1.27	0.19
31	20110308	0337	M1.5	S21E72	2768	8.46763	5.67	0.0000492	8.15	23.95	7.85	0.09
33	20110308	1808	M4.4	S17W88	848	0.00494	22.02	0.0023009	7.52	16.21	0.34	0.00
34	20110308	1946	M1.5	S19W87	6044	0.00313	8.75	0.0000175	9.16	16.40	0.27	20.96
37	20110309	2313	X1.5	N10W11	1660	0.04176	13.88	0.0776128	6.05	34.75	0.32	0.01
38	20110310	2234	M1.1	S25W86	1588	0.01840	7.67	0.0001338	7.66	5.74	3.12	0.56
40	20110314	1930	M4.2	N16W49	2308	0.21034	10.88	0.0041197	6.88	11.74	3.61	0.26
41	20110315	0018	M1.0	N11W83	1500	0.02256	8.97	0.0011179	5.04	4.58	4.85	3.10
46	20110422	0435	M1.8	S19E40	3124	0.00986	12.04	0.0006550	6.89	15.75	0.50	0.13
48	20110528	2109	M1.1	S21E70	2848	0.01151	11.79	0.0002199	7.07	11.97	0.82	0.00
50	20110607	0616	M2.5	S22W53	3608	5.21387	7.35	0.0019885	3.96	19.91	8.13	0.09
51	20110614	2136	M1.3	N14E77	2356	0.00375	10.90	0.0002383	7.37	12.63	0.43	1.63
52	20110727	1548	M1.1	N20E41	2004	0.00454	11.38	0.0000151	8.96	16.68	0.31	0.28
53	20110730	0204	M9.3	N16E35	1460	0.53662	17.06	0.0063472	7.86	16.20	3.55	0.11
55	20110803	0308	M1.1	N15W23	2760	0.00503	12.88	0.0002445	7.64	8.66	0.88	0.00
61	20110809	0748	X6.9	N20W69	2256	0.17734	25.80	0.2225979	7.38	28.85	0.86	0.39
63	20110905	0408	M1.6	N18W87	1516	0.00075	14.56	0.0000897	7.97	6.80	0.49	0.30
64	20110905	0727	M1.2	N18W87	2464	0.00236	14.00	0.0000076	8.38	5.55	1.18	1.41
65	20110906	0135	M5.3	N15W03	692	0.02325	10.01	0.0010473	8.42	19.15	0.58	0.05
68	20110908	1532	M6.7	N17W39	1764	0.11622	20.71	0.0022988	8.36	16.92	1.55	1.16
69	20110909	0601	M2.7	N14W48	1644	0.02375	9.37	0.0018086	7.23	17.19	0.68	0.09
70	20110909	1239	M1.2	N15W50	408	0.00262	11.99	0.0000095	9.44	8.41	0.66	1.41
71	20110910	0718	M1.1	N14W64	2488	0.00082	21.01	0.0001596	7.87	9.60	0.30	0.00
77	20110923	2348	M1.9	N12E56	1020	0.00323	10.26	0.0003025	7.46	15.63	0.29	0.06
81	20110924	1719	M3.1	N13E54	1324	0.01758	9.39	0.0007469	7.58	7.20	2.17	0.12
83	20110924	1909	M3.0	N15E50	1068	0.01551	8.75	0.0003280	7.79	23.56	0.34	0.69
84	20110924	2029	M5.8	N13E52	1180	0.08850	9.40	0.0119517	5.98	11.05	2.56	0.38

Table 2—Continued

ID	Date	Time	GOES class	Heliogr. position	Dur. flare τ_{flare} (s)	Emission measure EM_{49} (cm^{-3})	Temp. max. T_e (MK)	Photon flux I_1 (cm^2 s keV^{-1})	Spectral slope γ	Length scale L (Mm)	Density maximum n_{10} (cm^{-3})	Density preflare b_{10} (cm^{-3})
86	20110924	2345	M1.0	S28W66	1596	0.00126	13.44	0.0000355	7.78	6.99	0.61	0.28
91	20110925	1526	M3.7	N15E39	676	0.01059	8.55	0.0001207	8.83	13.64	0.65	3.75
98	20111002	0037	M3.9	N10W13	3696	0.01836	12.14	0.0005113	8.25	19.25	0.51	0.01
100	20111020	0310	M1.6	N18W88	1044	0.00580	19.18	0.0003065	7.98	7.15	1.26	0.03
101	20111021	1253	M1.3	N05W79	760	0.02016	7.03	0.0000893	7.04	6.49	2.72	0.02
103	20111031	1455	M1.1	N20E88	3980	0.00846	19.72	0.0007398	7.08	4.23	3.34	1.09
111	20111105	1110	M1.1	N22E43	2392	0.00081	17.51	0.0001009	7.74	8.28	0.38	0.21
116	20111115	0903	M1.2	N21W72	2448	0.00132	8.89	0.0000964	8.20	7.31	0.58	0.00
120	20111226	0213	M1.5	S18W34	2812	0.01884	7.57	0.0000523	7.93	13.91	0.84	0.38
122	20111229	1340	M1.9	S25E70	2368	0.00718	15.36	0.0000902	8.09	14.63	0.48	0.08
123	20111229	2143	M2.0	S25E67	632	0.00215	15.03	0.0002077	7.91	11.86	0.36	0.07
125	20111231	1309	M2.4	S25E46	1892	0.00399	20.88	0.0010953	7.05	8.39	0.82	2.09
126	20111231	1616	M1.5	S22E42	1272	0.00323	13.83	0.0001025	8.23	11.86	0.44	0.50
157	20120427	0815	M1.0	N13W26	732	0.00757	11.47	0.0000452	8.65	15.58	0.45	0.00
158	20120505	1319	M1.4	N11E78	200	0.00455	13.05	0.0009992	5.76	9.13	0.77	0.10
159	20120505	2256	M1.3	N11E73	624	0.02909	17.36	0.0011669	6.71	7.86	2.45	0.87
160	20120506	0112	M1.1	N11E73	1684	0.02905	3.53	0.0017250	5.94	6.80	3.04	3.19
167	20120510	0411	M5.7	N12E19	1128	0.01389	12.02	0.0196674	3.42	15.73	0.60	12.43
168	20120510	2020	M1.7	N12E10	1612	0.00354	12.89	0.0019588	6.47	11.93	0.46	0.10
169	20120517	0125	M5.1	N07W88	2708	0.07451	11.12	0.0002291	7.96	31.30	0.49	0.54
170	20120603	1748	M3.3	N15E33	852	0.08183	3.70	0.0009645	4.13	17.31	1.26	2.42
173	20120609	1645	M1.8	S16E76	1724	0.01346	7.86	0.0002785	8.03	7.50	1.79	0.09
176	20120614	1252	M1.9	S19E06	9628	0.02703	11.25	0.0011941	4.24	6.13	3.43	2.87
178	20120629	0913	M2.2	N15E37	696	0.03472	10.61	0.0001820	7.65	8.67	2.31	0.21
182	20120702	0026	M1.1	N15E01	1356	0.00326	12.41	0.0001100	7.72	10.32	0.54	0.85
187	20120704	0947	M5.3	S17W18	2416	0.02938	13.49	0.0078143	7.05	10.47	1.60	0.93
189	20120704	1435	M1.3	S18W20	428	0.02698	12.00	0.0022213	3.38	7.08	2.76	1.17
190	20120704	1633	M1.8	N14W33	828	0.01311	12.15	0.0041792	2.76	19.31	0.43	3.14
195	20120705	0325	M4.7	S18W29	1768	0.03276	9.85	0.0114881	6.97	8.49	2.31	0.75
196	20120705	0649	M1.1	S17W29	1208	0.00287	11.82	0.0002549	7.40	8.11	0.73	0.30
199	20120705	1139	M6.1	S18W32	1056	0.02275	12.28	0.0028190	6.09	15.74	0.76	0.24
200	20120705	1305	M1.2	S18W36	1400	0.00002	17.10	0.0003799	4.58	13.83	0.03	5.73
203	20120706	0137	M2.9	S18W43	2748	0.02383	12.65	0.0007113	8.18	8.49	1.97	0.22
205	20120706	0817	M1.5	S12W48	1392	0.01546	14.20	0.0027188	5.80	6.86	2.19	3.25
208	20120706	1848	M1.3	S15E88	1348	0.00546	14.39	0.0008365	7.04	10.17	0.72	0.43
210	20120707	0310	M1.2	S17W55	1664	0.00597	18.70	0.0009195	6.95	8.67	0.96	0.10
211	20120707	0818	M1.0	S16E76	684	0.00182	15.12	0.0000672	6.89	5.01	1.20	1.42
212	20120707	1057	M2.6	S17W59	520	0.01474	21.63	0.0022574	7.19	9.37	1.34	50.14
214	20120708	0944	M1.1	S16W70	768	0.00198	16.29	0.0001030	8.15	8.49	0.57	0.00
215	20120708	1206	M1.4	S16W72	160	0.01743	14.30	0.0029128	6.26	6.38	2.59	1.67
219	20120710	0605	M2.0	S16E30	1848	0.00205	18.43	0.0006706	7.18	9.37	0.50	0.50
223	20120719	0417	M7.7	S20W88	8532	0.11691	11.72	0.0023355	6.38	17.69	1.45	0.01
228	20120806	0433	M1.6	S14E88	728	0.04923	6.39	0.0022234	5.19	4.33	7.79	1.42
230	20120817	1312	M2.4	N18E88	1512	0.05884	17.53	0.0006027	7.62	4.99	6.88	0.92

Table 2—Continued

ID	Date	Time	GOES class	Heliogr. position	Dur. flare τ_{flare} (s)	Emission measure EM_{49} (cm^{-3})	Temp. max. T_e (MK)	Photon flux I_1 (cm^2 s keV^{-1})	Spectral slope γ	Length scale L (Mm)	Density maximum n_{10} (cm^{-3})	Density preflare b_{10} (cm^{-3})
235	20120818	2246	M1.0	N18E88	1036	0.00188	12.60	0.0000531	8.48	8.99	0.51	0.33
238	20120906	0406	M1.6	N04W61	2184	0.01730	22.22	0.0000244	9.41	9.46	1.43	5.75
241	20120930	0427	M1.3	N12W81	2228	0.00236	9.32	0.0009274	7.16	4.94	1.40	22.21
245	20121020	1805	M9.0	S12E88	2116	0.08375	10.51	0.0036557	8.14	9.81	2.98	0.25
246	20121021	1946	M1.3	S13E78	2124	0.01076	19.52	0.0004559	7.47	9.81	1.07	0.14
248	20121023	0313	X1.8	S13E58	1380	0.01599	26.74	0.0562808	6.90	10.40	1.19	0.00
251	20121112	2313	M2.0	S25E48	2124	0.03314	8.28	0.0002480	8.21	8.45	2.34	1.33
253	20121113	0542	M2.5	S26E44	1396	0.02954	21.22	0.0003934	8.13	10.06	1.70	1.22
255	20121114	0359	M1.1	S23E27	1352	0.03191	6.93	0.0014156	3.44	5.17	4.81	3.19
257	20121120	1921	M1.6	N10E19	372	0.04471	7.90	0.0007343	4.91	8.61	2.65	0.18
258	20121121	0645	M1.4	N10E12	932	0.02454	9.04	0.0008045	6.36	11.93	1.20	0.08
261	20121127	2105	M1.0	S13W42	1668	0.00753	14.83	0.0001938	7.99	7.09	1.45	0.22
262	20121128	2120	M2.2	S12W56	3044	0.03893	19.23	0.0007241	7.00	12.86	1.35	0.17
264	20130111	0843	M1.2	N05E42	1180	0.00542	7.63	0.0003004	7.00	7.66	1.10	0.00
266	20130113	0045	M1.0	N18W15	764	0.01716	7.39	0.0011418	6.06	6.18	2.70	31.98
268	20130217	1545	M1.9	N12E23	620	0.01225	8.89	0.0000633	8.87	4.87	3.26	2.45
271	20130321	2142	M1.6	N09W88	3516	0.03346	12.18	0.0000383	8.23	12.28	1.34	0.12
273	20130411	0655	M6.5	N11E13	1076	0.04168	11.42	0.0018528	5.27	25.55	0.50	0.91
274	20130412	1952	M3.3	N21W47	2012	0.02328	18.80	0.0013568	7.29	13.87	0.93	0.18
276	20130502	0458	M1.1	N10W19	2380	0.00017	19.42	0.0007521	4.69	8.24	0.17	0.00
277	20130503	1639	M1.3	N11W38	2872	0.00010	18.37	0.0009633	5.20	3.04	0.59	0.37
278	20130503	1724	M5.7	N15E83	1316	0.03689	22.67	0.0033001	6.85	13.27	1.26	0.07
283	20130512	2237	M1.2	N10E89	1872	0.00186	20.36	0.0014919	6.05	11.68	0.34	0.15
284	20130513	0153	X1.7	N11E89	2496	0.10615	12.49	0.0132431	7.65	16.33	1.56	0.11
285	20130513	1157	M1.3	N10E89	1048	0.00403	23.26	0.0014927	6.72	3.52	3.04	0.00
288	20130515	0125	X1.2	N10E68	3524	0.09999	11.15	0.0031250	8.06	22.63	0.93	0.83
289	20130516	2136	M1.3	N11E40	1280	0.00133	20.44	0.0000784	8.12	7.27	0.59	0.15
291	20130520	0516	M1.7	N09E89	1380	0.01296	12.50	0.0000855	8.06	8.08	1.57	1.98
292	20130522	1308	M5.0	N14W87	3248	0.04485	11.64	0.0011678	4.63	20.27	0.73	0.18
293	20130531	1952	M1.0	N12E42	1060	0.00112	11.25	0.0000235	8.27	9.35	0.37	0.06
297	20130623	2048	M2.9	S18E63	1132	0.02889	6.25	0.0007958	7.29	5.01	4.79	0.06
298	20130703	0700	M1.5	S14E82	1548	0.01205	22.27	0.0000406	8.91	9.38	1.21	0.13
299	20130812	1021	M1.5	S21E17	1536	0.00450	12.44	0.0000636	8.64	11.58	0.54	1.24
303	20131011	0701	M1.5	N21E87	1124	0.01884	17.17	0.0002881	5.13	3.48	6.69	0.64
304	20131013	0012	M1.7	S22E17	1416	0.67760	11.05	0.0001016	6.80	9.52	8.86	2.12
307	20131017	1509	M1.2	S09W63	1696	0.00352	11.69	0.0000092	9.04	10.42	0.56	0.07
308	20131022	0014	M1.0	N08E20	1068	0.00014	21.27	0.0003649	6.90	8.32	0.15	0.00
311	20131023	2041	M2.7	N08W06	3368	0.01733	18.16	0.0008089	6.76	9.50	1.42	3.60
312	20131023	2333	M1.4	N09W08	2000	0.01171	15.02	0.0001602	5.42	6.49	2.07	0.24
313	20131023	2358	M3.1	N09W09	452	0.00031	21.46	0.0003714	7.34	8.84	0.21	0.00
317	20131025	0248	M2.9	S07E76	3164	0.03163	18.68	0.0004501	7.18	12.85	1.22	0.94
318	20131025	0753	X1.7	S08E73	676	0.04461	33.74	0.0298859	7.58	11.36	1.74	0.17
320	20131025	1451	X2.1	S06E69	3568	0.10233	11.35	0.0003450	10.39	16.98	1.45	0.54
321	20131025	1702	M1.3	S08E67	2052	0.01089	15.70	0.0008598	5.99	7.14	1.73	1.22

Table 2—Continued

ID	Date	Time	GOES class	Heliogr. position	Dur. flare τ_{flare} (s)	Emission measure EM_{49} (cm^{-3})	Temp. max. T_e (MK)	Photon flux I_1 (cm^2 s keV^{-1})	Spectral slope γ	Length scale L (Mm)	Density maximum n_{10} (cm^{-3})	Density preflare b_{10} (cm^{-3})
325	20131026	0917	M1.5	S08E59	1060	0.00078	11.77	0.0001197	6.67	6.48	0.54	0.08
328	20131026	1949	M1.0	S08E51	1940	0.00004	20.02	0.0001241	6.61	3.87	0.25	0.00
334	20131028	1446	M2.7	S08E27	2600	0.00557	19.67	0.0006088	7.57	23.10	0.21	0.07
336	20131028	2048	M1.5	N07W83	1748	0.00481	8.04	0.0002001	7.99	6.48	1.33	1.22
340	20131102	2213	M1.6	S12W12	768	0.00239	8.99	0.0002536	7.73	5.47	1.21	0.19
343	20131105	1808	M1.0	S12E47	1124	0.00159	6.43	0.0001669	7.77	4.57	1.29	5.16
345	20131106	1339	M3.8	S09E35	1936	0.00399	9.70	0.0031537	6.63	7.92	0.90	0.15
347	20131107	0334	M2.3	S08E26	1436	0.02208	3.12	0.0064472	5.08	12.92	1.01	0.04
351	20131110	0508	X1.1	S11W17	3284	0.04878	21.66	0.0079130	7.69	22.03	0.68	0.20
352	20131111	1101	M2.4	S17E74	3068	0.00399	19.31	0.0002777	7.71	10.35	0.60	0.10
353	20131113	1457	M1.4	S20E46	1400	0.00130	20.16	0.0001988	7.48	14.63	0.20	0.07
354	20131115	0220	M1.0	N07E53	1252	0.00109	20.12	0.0001849	7.62	9.28	0.37	0.03
357	20131117	0506	M1.0	S19W41	1208	0.00089	6.36	0.0002105	7.49	2.98	1.84	0.46
359	20131121	1052	M1.2	S14W89	1248	0.02074	16.89	0.0004123	4.71	4.55	4.69	2.51
360	20131123	0220	M1.1	N13W58	2584	0.00110	17.26	0.0000888	7.99	5.71	0.77	0.25
363	20131219	2306	M3.5	S16E89	2304	0.01275	21.85	0.0004127	8.06	15.14	0.61	0.04
364	20131220	1135	M1.6	S16E78	4272	0.00332	15.97	0.0001171	6.64	7.27	0.93	0.58
365	20131222	0805	M1.9	S17W51	1788	0.00701	18.95	0.0003829	7.68	5.42	2.10	0.25
366	20131222	0833	M1.1	S17W52	1956	0.00852	15.06	0.0004831	4.45	6.18	1.90	0.28
367	20131222	1424	M1.6	S16E44	2532	0.03249	11.35	0.0004446	6.57	9.85	1.84	0.06
368	20131222	1506	M3.3	S17W55	1328	0.00742	21.78	0.0003082	7.26	13.71	0.54	0.37
377	20140103	1241	M1.0	S04E52	1000	0.02158	7.58	0.0004308	4.84	3.83	6.20	2.66
382	20140107	0349	M1.0	N07E07	1432	0.00661	7.25	0.0007455	6.14	4.20	2.99	0.39
385	20140108	0339	M3.6	N11W88	2016	0.01548	19.24	0.0020340	6.89	3.83	5.25	0.52
386	20140113	2148	M1.3	S08W75	660	0.00086	7.92	0.0019242	6.65	2.97	1.81	0.39
387	20140127	0105	M1.0	S16E88	2860	0.00172	16.77	0.0002649	4.60	11.25	0.35	0.03
389	20140127	2205	M4.9	S14E88	1880	0.00078	24.20	0.0041016	6.96	4.85	0.83	61.62
393	20140128	1233	M1.3	S15E79	1708	0.00363	5.90	0.0000335	8.80	4.85	1.78	0.00
395	20140128	2204	M2.6	S14E74	1112	0.00399	7.01	0.0021642	6.82	5.69	1.47	0.79

Table 3.   Low-energy cutoff energies and total nonthermal energies calculated for 4 models (en, wt, tof, co), derived from the observables of 143 M and X-class flare events, tabulated in Table 2.

ID	Cutoff energy ε_{en} (keV)	Cutoff energy ε_{wt} (keV)	Cutoff energy ε_{tof} (keV)	Cutoff energy ε_{co} (keV)	Nonthermal energy E_{en} (10^{30} erg)	Nonthermal energy E_{wt} (10^{30} erg)	Nonthermal energy E_{tof} (10^{30} erg)	Nonthermal energy E_{co} (10^{30} erg)
1	1.00	4.80	6.70	15.00	0.7778	0.0042	0.0015	0.0001
2	3.20	6.60	1.70	19.00	0.0305	0.0017	0.4079	0.0000
3	0.70	5.30	1.90	30.00	21.5602	0.0497	1.2021	0.0002
4	11.50	14.20	11.20	21.00	2.2251	0.4854	2.6257	0.0307
10	16.20	13.40	9.00	30.00	1.4205	4.5095	49.6561	0.0333
12	12.80	14.80	15.10	27.00	46.3275	19.9327	17.1499	0.5138
13	8.70	12.60	5.90	21.00	2.4624	0.2781	23.6050	0.0143
15	9.20	8.90	9.90	22.00	5.1154	6.0449	3.1357	0.0165
16	14.90	6.90	15.50	27.00	2.5982	312.6780	2.0072	0.0636
18	10.50	9.60	10.90	24.00	0.8962	1.6026	0.7330	0.0057
19	1.90	3.20	9.70	15.00	0.3648	0.0681	0.0017	0.0004
20	10.70	5.80	10.40	22.00	2.0033	143.3275	2.4943	0.0132
21	9.90	9.60	7.50	15.00	5.4652	7.0165	52.4010	0.1755
22	7.60	5.50	5.30	22.00	5.5665	35.2264	41.2397	0.0164
23	9.80	5.80	6.40	20.00	3.4690	90.9612	49.9326	0.0367
28	5.40	5.60	4.50	15.00	6.6379	5.5572	14.3126	0.0957
29	12.90	6.00	5.20	26.00	0.1107	4.2193	8.2575	0.0039
30	9.20	2.70	9.60	22.00	0.9000	895.5553	0.7023	0.0063
31	7.90	4.50	38.30	30.00	16.7310	975.3401	0.0002	0.0012
33	29.20	16.20	6.60	21.00	0.0294	1.3916	495.0242	0.2530
34	6.10	7.70	5.80	15.00	416.3836	68.0520	624.6119	0.2839
37	12.80	8.40	9.30	28.00	5.1082	41.4942	25.9488	0.0969
38	10.00	5.70	11.80	20.00	0.6242	26.0680	0.2079	0.0063
40	11.30	7.40	18.20	30.00	3.8600	47.7786	0.2403	0.0126
41	4.10	4.70	13.20	15.00	1.1429	0.6713	0.0102	0.0060
46	8.80	8.20	7.90	20.00	7.1019	10.9290	13.8560	0.0568
48	96.70	8.20	8.80	16.00	0.0000	5.1251	3.4567	0.0888
50	2.00	3.10	35.60	12.00	2.7037	0.6692	0.0005	0.0127
51	6.60	7.90	6.50	12.00	14.6050	4.8811	16.0264	0.3311
52	8.10	9.80	6.40	15.00	10.3822	2.4438	71.7504	0.0802
53	14.20	13.00	21.20	15.00	5.3108	9.4608	0.3361	3.6127
55	54.60	9.60	7.70	19.00	0.0001	5.8205	24.7286	0.0624
61	14.50	18.60	13.90	28.00	106.4098	21.3920	137.7906	1.5931
63	10.40	11.30	5.10	18.00	1.3532	0.7893	198.1350	0.0300
64	8.10	11.30	7.10	30.00	2.6708	0.2223	6.7030	0.0002
65	12.00	8.10	9.30	30.00	22.9111	404.4191	152.0502	0.0251
68	10.50	16.70	14.30	18.00	101.2172	3.2939	10.3612	1.9095
69	10.50	6.70	9.60	16.00	9.9118	168.5142	17.3350	0.7104
70	7.60	10.80	6.60	17.00	19.8497	1.0888	68.6569	0.0234
71	21.20	16.10	4.80	30.00	0.0204	0.1367	570.6394	0.0019
77	9.00	7.50	6.00	15.00	3.5533	11.7135	50.8674	0.1313
81	13.40	6.90	11.00	23.00	0.7741	59.5029	2.8106	0.0225
83	6.30	6.60	8.00	14.00	98.3267	65.8536	19.0484	0.4112
84	8.60	5.70	14.90	29.00	6.2511	51.7382	0.4210	0.0151

Table 3—Continued

ID	Cutoff energy ε_{en} (keV)	Cutoff energy ε_{wt} (keV)	Cutoff energy ε_{tof} (keV)	Cutoff energy ε_{co} (keV)	Nonthermal energy E_{en} (10^{30} erg)	Nonthermal energy E_{wt} (10^{30} erg)	Nonthermal energy E_{tof} (10^{30} erg)	Nonthermal energy E_{co} (10^{30} erg)
86	8.80	10.20	5.80	28.00	1.7223	0.6667	31.8594	0.0007
91	7.00	7.20	8.30	12.00	135.1171	107.9637	37.2981	2.0702
98	15.90	9.70	8.70	20.00	1.0634	39.2940	82.8666	0.2042
100	14.90	14.90	8.40	20.00	0.6826	0.7121	38.6946	0.0894
101	11.20	4.90	11.70	15.00	0.0898	13.9602	0.0692	0.0157
103	12.80	13.70	10.50	28.00	0.9179	0.5842	2.9818	0.0077
111	10.30	13.20	4.90	22.00	1.4515	0.2686	201.8147	0.0086
116	23.70	7.10	5.80	14.00	0.0077	47.6822	205.9947	0.3427
120	7.70	5.80	9.50	15.00	6.5091	44.8960	1.4804	0.0639
122	10.00	12.00	7.40	27.00	2.4833	0.6709	21.1648	0.0022
123	9.90	11.50	5.80	28.00	4.1542	1.4337	172.7290	0.0031
125	8.20	14.50	7.30	26.00	6.0413	0.1924	11.8059	0.0056
126	8.40	11.00	6.40	22.00	13.1490	1.9445	99.5300	0.0130
157	36.50	9.50	7.40	14.00	0.0001	3.0211	21.6221	0.1610
158	5.30	7.60	7.40	15.00	1.3581	0.2412	0.2706	0.0095
159	7.30	11.50	12.30	17.00	7.0812	0.5296	0.3739	0.0578
160	5.90	2.10	12.70	17.00	3.0419	473.1884	0.0663	0.0157
167	0.40	4.60	8.60	21.00	30.2518	0.0892	0.0196	0.0022
168	9.70	8.30	6.50	15.00	1.7269	4.1018	15.3409	0.1610
169	6.60	8.60	11.00	15.00	110.4820	16.9623	3.0718	0.3498
170	0.70	1.60	13.00	14.00	19.2109	1.2400	0.0019	0.0015
173	13.90	6.10	10.20	20.00	0.4422	140.1815	3.7789	0.0338
176	2.90	5.10	12.80	15.00	0.5684	0.0932	0.0047	0.0028
178	9.10	7.90	12.50	19.00	1.6227	3.9857	0.1907	0.0118
182	7.30	9.30	6.60	30.00	10.8205	2.1517	21.4655	0.0008
187	11.40	9.40	11.40	22.00	10.0191	33.7559	10.0593	0.1921
189	0.60	4.50	12.30	16.00	0.6845	0.0060	0.0006	0.0003
190	0.10	3.90	8.00	14.00	4.6077	0.0036	0.0010	0.0004
195	12.80	6.80	12.40	24.00	4.9962	219.9091	5.9444	0.1149
196	9.30	8.60	6.80	22.00	3.5504	6.0006	25.6911	0.0142
199	6.30	7.50	9.70	18.00	5.3694	2.2979	0.6250	0.0267
200	1.00	8.20	1.80	15.00	40.7531	0.0202	5.0761	0.0024
203	14.50	10.00	11.40	21.00	0.4537	6.5307	2.5106	0.0320
205	5.70	8.30	10.80	22.00	5.8572	0.9418	0.2667	0.0089
208	8.60	10.00	7.60	24.00	6.2984	2.6349	14.0258	0.0131
210	11.70	12.80	8.10	24.00	0.4536	0.2598	4.1385	0.0062
211	5.90	10.30	6.90	30.00	2.0414	0.0798	0.8681	0.0001
212	4.90	15.30	9.90	24.00	505.2834	0.4216	6.1786	0.0257
214	19.60	12.80	6.10	30.00	0.0259	0.5373	105.4782	0.0012
215	5.70	8.90	11.40	17.00	8.9478	0.8496	0.2419	0.0290
219	9.30	13.00	6.00	30.00	7.8497	0.9755	110.5648	0.0055
223	14.80	7.50	14.20	16.00	0.7552	30.5329	0.9672	0.5032
228	5.40	3.40	16.20	15.00	0.7626	5.0530	0.0073	0.0101
230	11.90	13.00	16.40	18.00	0.7520	0.4090	0.0897	0.0480

Table 3—Continued

ID	Cutoff energy ε_{en} (keV)	Cutoff energy ε_{wt} (keV)	Cutoff energy ε_{tof} (keV)	Cutoff energy ε_{co} (keV)	Nonthermal energy E_{en} (10^{30} erg)	Nonthermal energy E_{wt} (10^{30} erg)	Nonthermal energy E_{tof} (10^{30} erg)	Nonthermal energy E_{co} (10^{30} erg)
235	9.40	10.30	6.00	30.00	2.7705	1.4368	84.1892	0.0005
238	8.30	19.90	10.30	17.00	26.7858	0.0172	4.5569	0.0661
241	7.60	6.60	7.30	16.00	9.4226	23.5095	11.6637	0.0967
245	15.90	8.30	15.10	20.00	2.5768	276.5678	3.7736	0.5087
246	11.40	14.30	9.00	22.00	1.3530	0.3115	5.9178	0.0188
248	194.30	18.20	9.80	30.00	0.0000	0.9979	37.5929	0.0524
251	10.00	6.60	12.40	22.00	5.8906	121.1315	1.2253	0.0201
253	9.40	16.70	11.60	20.00	10.7416	0.1714	2.3528	0.0474
255	0.80	2.60	13.90	14.00	0.1509	0.0085	0.0001	0.0001
257	3.20	4.00	13.30	16.00	0.9894	0.3824	0.0035	0.0017
258	7.70	5.70	10.60	17.00	3.0739	14.6470	0.5495	0.0434
261	11.90	11.50	9.00	24.00	0.6241	0.8022	4.5538	0.0047
262	9.70	13.30	11.70	17.00	2.8245	0.4292	0.9263	0.0964
264	32.10	5.30	8.10	18.00	0.0016	80.4219	6.0352	0.0504
266	3.60	4.50	11.40	15.00	24.2342	8.1539	0.0734	0.0184
268	9.70	7.60	11.10	30.00	2.4258	17.6247	0.8419	0.0003
271	9.90	9.70	11.40	14.00	3.0094	3.6091	1.1474	0.2522
273	2.30	6.20	10.00	12.00	83.7943	1.2304	0.1574	0.0719
274	10.40	13.40	10.10	16.00	13.3241	2.7140	16.7779	0.9044
276	52.20	9.50	3.30	16.00	0.0001	0.0280	1.3581	0.0041
277	9.50	9.80	3.70	21.00	0.1121	0.0971	5.6071	0.0040
278	11.60	15.30	11.40	20.00	3.1159	0.5936	3.3443	0.1256
283	7.80	12.40	5.60	29.00	1.1321	0.1071	5.9789	0.0014
284	15.80	9.30	14.10	25.00	14.9141	511.5092	32.2520	0.7191
285	77.60	15.50	9.10	28.00	0.0000	0.1121	2.2906	0.0038
288	10.30	8.70	12.80	18.00	70.1435	233.2775	15.2921	1.3882
289	11.10	16.10	5.80	30.00	1.2008	0.0851	122.8816	0.0010
291	7.80	9.80	9.90	15.00	10.7964	2.1221	1.8687	0.1025
292	2.60	5.60	10.80	14.00	8.6450	0.5070	0.0486	0.0188
293	9.80	9.00	5.20	24.00	0.6634	1.2131	65.5062	0.0010
297	15.80	4.50	13.70	15.00	0.1384	394.0855	0.3433	0.1936
298	11.60	19.00	9.40	16.00	1.5009	0.0292	7.6938	0.1153
299	8.20	10.30	7.00	15.00	15.9317	2.7585	56.0776	0.1611
303	5.00	9.10	13.50	17.00	0.2404	0.0207	0.0040	0.0016
304	4.80	7.40	25.70	30.00	8.2187	0.6604	0.0005	0.0002
307	10.50	10.10	6.70	23.00	2.4395	3.3935	89.3478	0.0046
308	39.30	14.50	3.20	30.00	0.0002	0.0829	654.5867	0.0011
311	6.80	12.20	10.30	21.00	21.6912	0.7447	1.9624	0.0318
312	5.00	8.30	10.20	21.00	0.1779	0.0181	0.0072	0.0003
313	20.70	15.40	3.80	30.00	0.0136	0.0883	606.1953	0.0013
317	7.60	13.20	11.10	20.00	20.5291	0.6779	1.9889	0.0513
318	16.00	25.00	12.40	30.00	10.2022	0.5564	54.3011	0.1656
320	14.60	11.10	13.80	30.00	14.5203	178.0020	23.1600	0.0163
321	6.30	9.50	9.80	16.00	1.8441	0.2419	0.2003	0.0176

Table 3—Continued

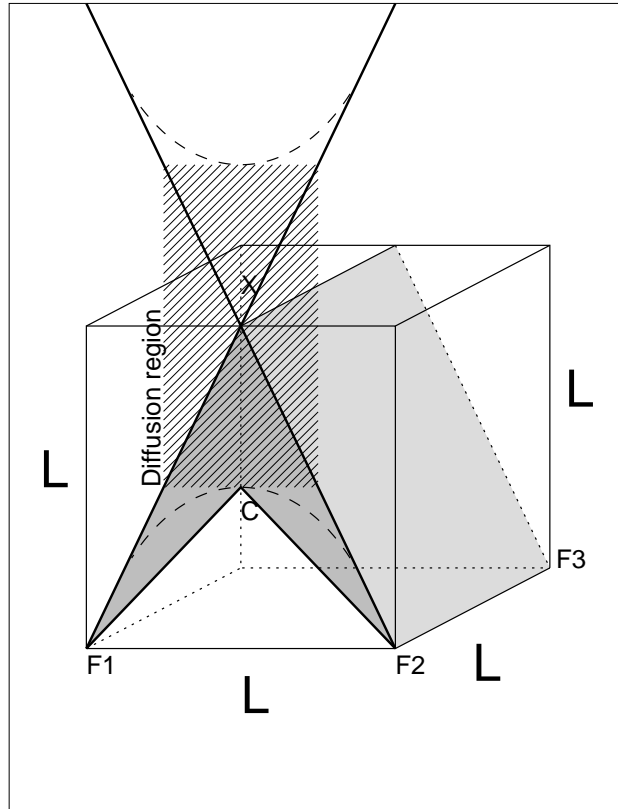| ID	Cutoff energy ε_{en} (keV)	Cutoff energy ε_{wt} (keV)	Cutoff energy ε_{tof} (keV)	Cutoff energy ε_{co} (keV)	Nonthermal energy E_{en} (10^{30} erg)	Nonthermal energy E_{wt} (10^{30} erg)	Nonthermal energy E_{tof} (10^{30} erg)	Nonthermal energy E_{co} (10^{30} erg)
325	8.70	7.80	5.20	20.00	0.5292	1.0053	9.8712	0.0048
328	26.10	13.10	2.70	30.00	0.0003	0.0150	97.9885	0.0001
334	9.70	14.50	6.20	21.00	4.4813	0.3091	84.4325	0.0276
336	10.00	6.20	8.20	17.00	2.2796	64.5426	9.3836	0.0578
340	11.80	6.80	7.20	17.00	0.7679	32.6484	21.8765	0.0662
343	8.30	4.90	6.80	21.00	3.3767	129.3156	13.4555	0.0064
345	12.80	6.40	7.40	21.00	1.1343	57.4849	24.0198	0.0702
347	7.40	1.60	10.10	14.00	0.7488	361.8527	0.2138	0.0565
351	12.80	16.20	10.80	20.00	10.7767	2.1711	33.3844	0.5354
352	12.10	14.50	7.00	23.00	2.4294	0.7171	98.3107	0.0324
353	9.00	14.70	4.80	27.00	4.3452	0.1747	244.4080	0.0035
354	12.20	15.00	5.20	26.00	0.5077	0.1293	145.9955	0.0033
357	13.10	4.70	6.50	15.00	0.1348	109.7154	12.1532	0.0556
359	2.70	8.30	12.90	15.00	2.9134	0.0436	0.0085	0.0049
360	12.20	13.40	5.90	15.00	1.2240	0.6325	201.4743	0.2834
363	12.70	17.10	8.50	21.00	2.8401	0.3577	50.4921	0.0826
364	7.40	10.50	7.30	17.00	1.8018	0.2566	2.0618	0.0171
365	13.30	14.20	9.40	22.00	0.3626	0.2367	3.6241	0.0126
366	3.30	7.10	9.60	15.00	0.1169	0.0084	0.0030	0.0006
367	10.10	7.40	11.90	14.00	0.7798	4.3741	0.3099	0.1260
368	7.30	15.50	7.60	22.00	7.7331	0.0665	5.8546	0.0074
377	3.10	3.80	13.60	16.00	0.6630	0.3083	0.0023	0.0013
382	9.70	4.50	9.90	17.00	0.1497	7.9724	0.1325	0.0082
385	14.80	13.10	12.50	16.00	0.4465	0.9144	1.1817	0.2800
386	13.70	5.20	6.50	15.00	0.1604	36.7204	10.8544	0.0947
387	3.80	8.10	5.50	15.00	0.3818	0.0258	0.1018	0.0028
389	7.50	16.60	5.60	30.00	39.5556	0.3435	224.5840	0.0101
393	25.90	5.00	8.20	30.00	0.0023	900.0698	18.1551	0.0007
395	10.60	4.70	8.10	18.00	3.1501	350.3838	15.3367	0.1457

Fig. 1.— Geometric model of a flare arcade embedded in a cube with length L, width $w = L$, and height $h = L$, with volume $V = L \times w \times h = L^3$. The footpoints of the loop arcade are at the locations $F1$ and $F2$, the X-point X at height $h = L$, and the cusp C at height $L/2$. The magnetic field line through the cusp is approximated with the triangle $F1 - C - F2$ and has the volume $V = L^3 \times q_{geo}$, where the geometric filling factor of the cube is $q_{geo} = 1/4$. The diffusion region of magnetic reconnection in the X-point is indicated with a shaded area and has the same filling factor of $q_{geo} = 1/4$.
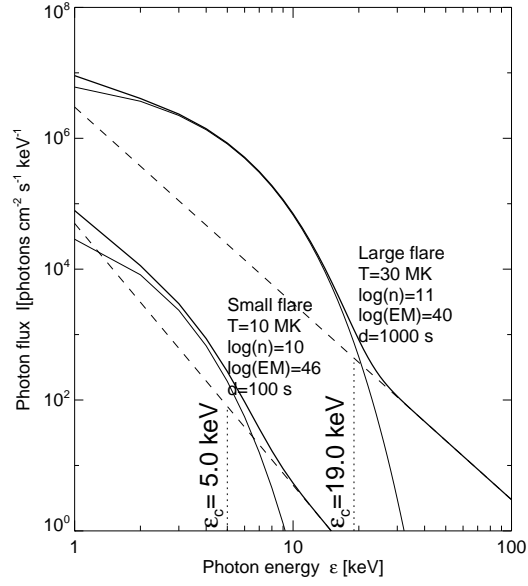
Fig. 2.— Theoretical hard X-ray spectrum consisting of a thermal and a nonthermal (power law) component with equal energy content above the cutoff energy ε_c. The parameters are chosen for a large flare with $T_e = 30$ MK, $n_e = 10^{11}$ cm^{-3}, $EM_V = 10^{49}$ cm^{-3}, $\gamma = 3$, and duration $\tau_{flare} = 1000$ s; and for a small flare with $T_e = 10$ MK, $n_e = 10^{10}$ cm^{-3}, $EM_V = 10^{46}$ cm^{-3}, $\gamma = 5$, and duration $\tau_{flare} = 100$ s. The x-axis is the photon energy in units of keV.
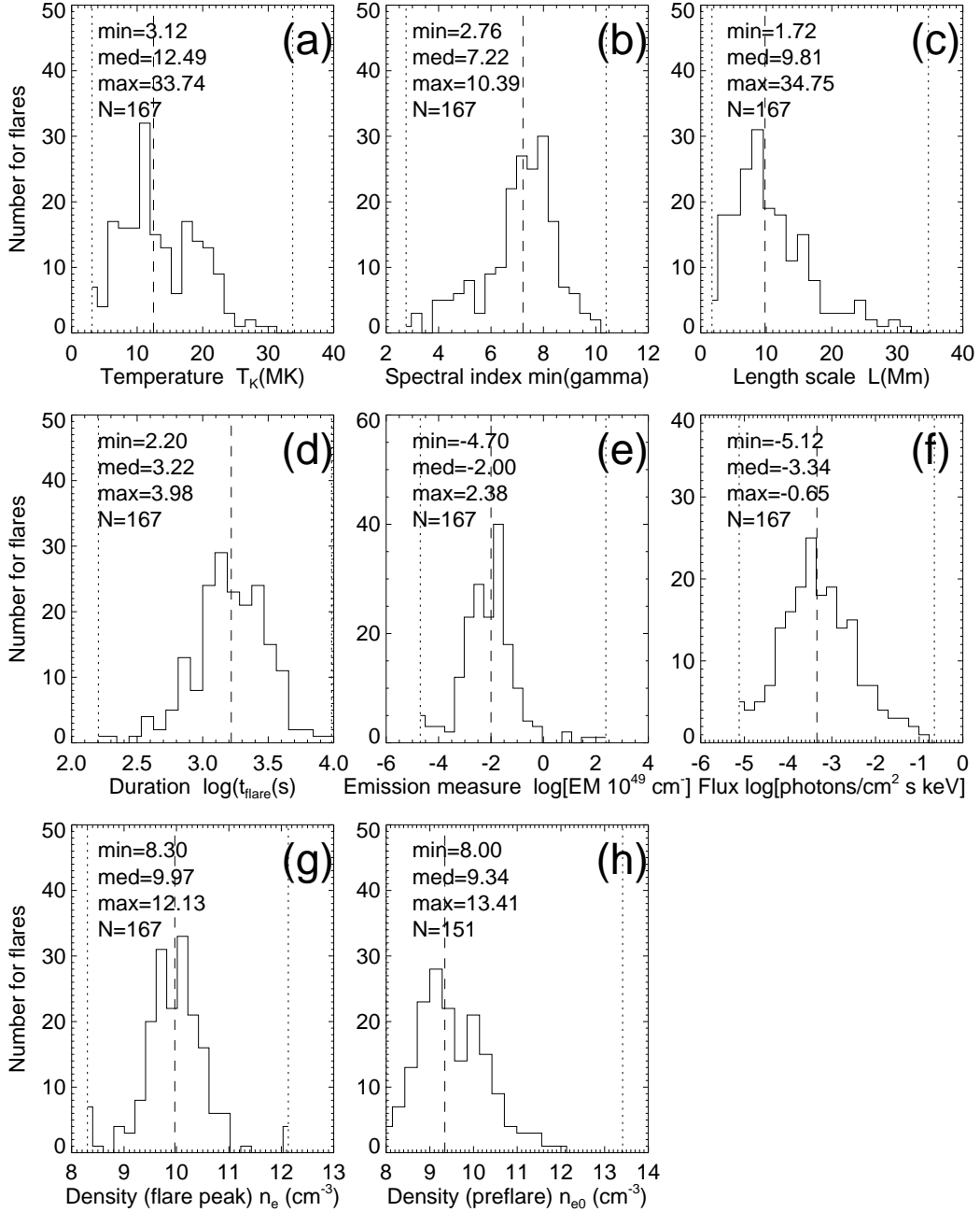
Fig. 3.— The distributions of measured observables are shown, which are required in modeling of the low-energy cutoff of hard X-ray spectra of M and X-class flares. The minimum, maximum and median values are indicated.
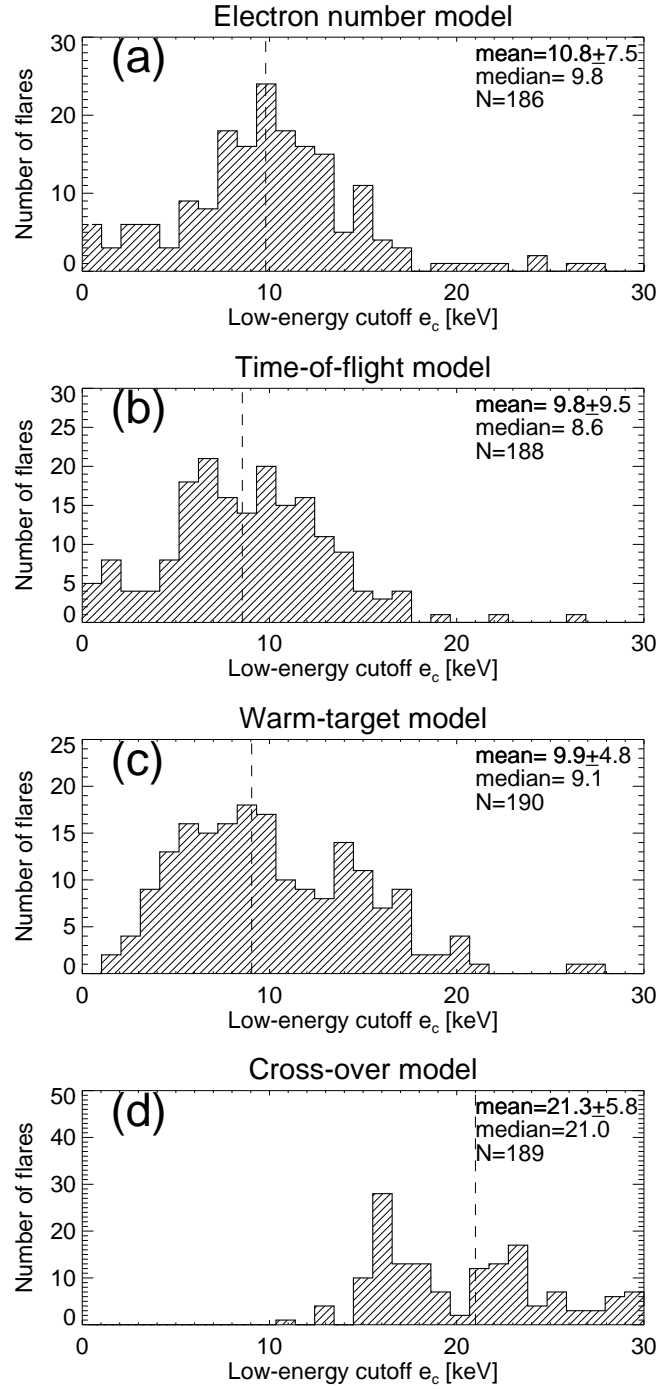
Fig. 4.— Distribution of low-energy cutoffs in four models: the electron number model (a), the time-of-flight model (b), the warm target model (c), and the cross over model (d). Note that the first three models all yield a low-energy cutoff energy of $e_c \approx 10$ keV, while the cross-order model predicts upper limits only, at $e_c \approx 21$ keV.
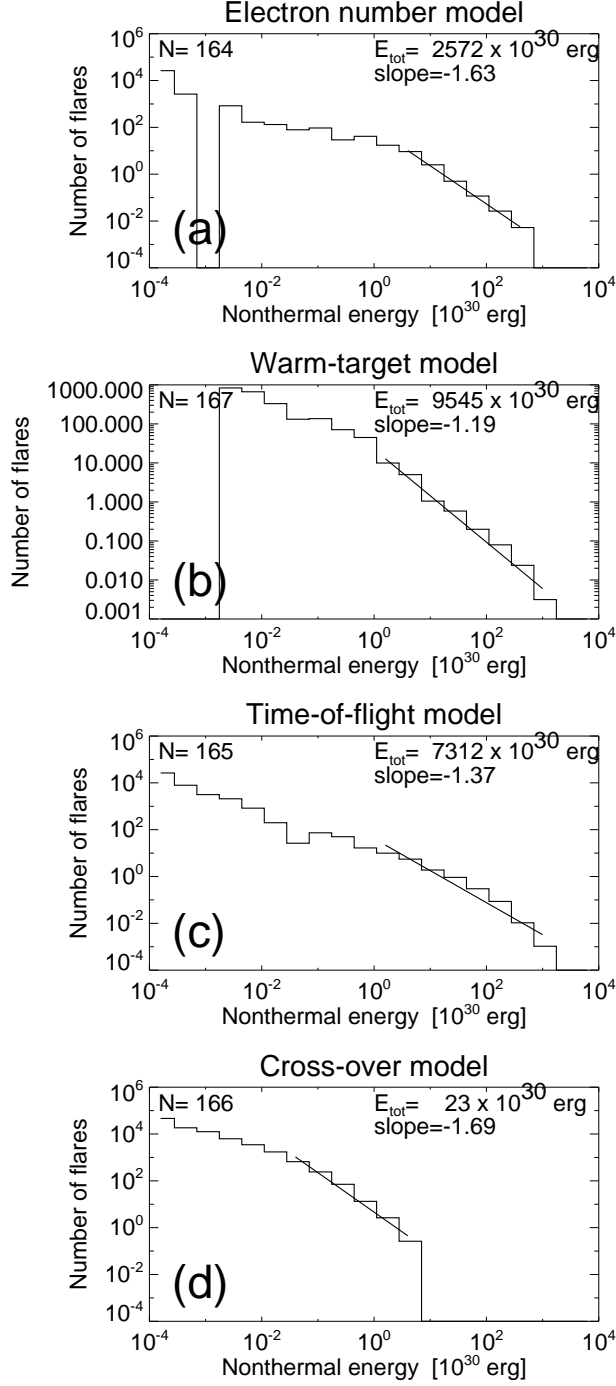
Fig. 5.— Size distributions of nonthermal energies E_{nth} (histograms with power law fits) and total nonthermal energy E_{tot} contained in each distribution for 4 different models of the low-energy cutoff e_c.
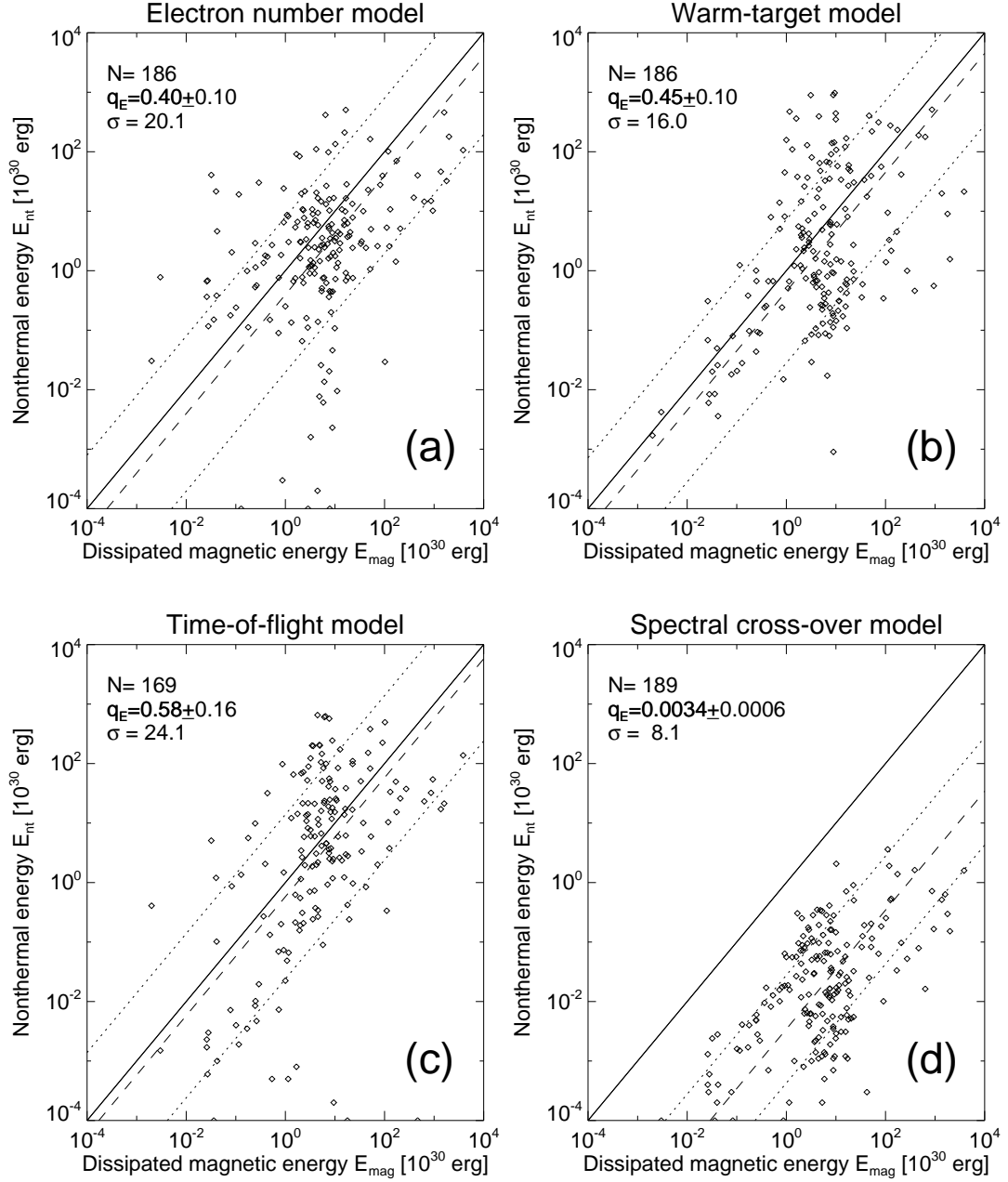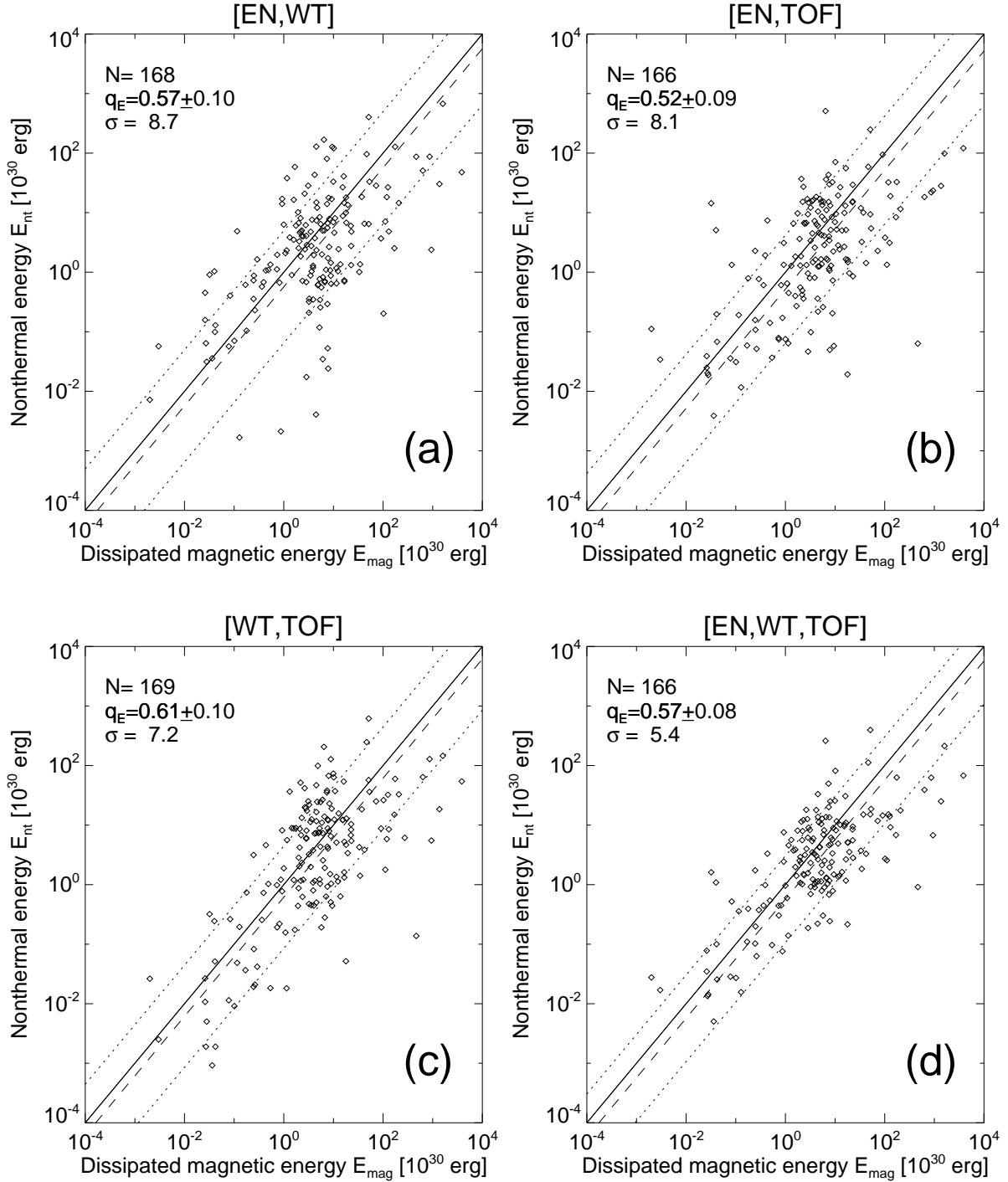
Fig. 6.— Scatterplots of nonthermal energy in accelerated electrons (E_{nth}) as a function of the dissipated magnetic energy (E_{diss}). Equivalence is rendered with a solid diagonal line, the logarithmically averaged ratios (q_E) with a dashed line, and the standard deviation factors (σ) with dotted lines.

Fig. 7.— Scatterplots of nonthermal energy in accelerated electrons (E_{nth}) as a function of the dissipated magnetic energy (E_{diss}), averaged from two or three methods: (a) [EN,WT], (b) [EN, TOF], (c) [WT, TOF], and (d) [EN, WT, TOF], with similar representation as Fig. 6/ Note that the logarithmically averaged ratios are compatible with the previous result of $E_{nth}/E_{diss} = 0.51 \pm 0.17$ (Aschwanden et al. (2017).
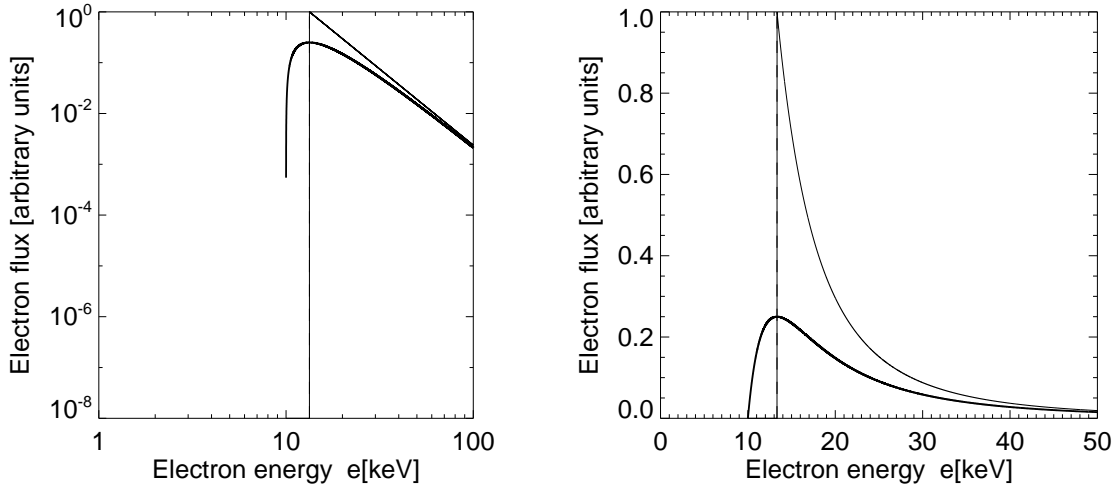
Fig. 8.— Electron injection spectrum with a smooth low-energy cutoff at the lower end (thick linestyle), asymptotically approaching a power law function at the upper end (as defined in Eq. A1), rendered on a log-log scale (left panel), as well as on a linear scale (right panel). The power law slope of the electron injection spectrum is $\delta = 3$, the minimum energy is $\varepsilon_{min} = 10$ keV, the peak energy is $\varepsilon_{peak} = 13.3$ keV, with ratio $\varepsilon_{peak}/\varepsilon_{min} = (1 + 1/\delta) = 4/3$.